Creation and Optimization of Modulation Tranfer Spectroscopy Error Signals from the 5S to 6P Transition in Rubidium

Chris Nowaczek

Bachelorarbeit in Physik
angefertigt im Institut für Angewandte Physik

vorgelegt der
Mathematisch-Naturwissenschaftlichen Fakultät
der
Rheinischen Friedrich-Wilhelms-Universität
Bonn

January 2025

Ich versichere, dass ich diese Arbeit selbstständig verfasst und keine anderen als die angegebenen Quellen und Hilfsmittel benutzt sowie die Zitate kenntlich gemacht habe.

Bonn, 29.01.2025. .....

Datum Unterschrift

1. Gutachter: Prof. Dr. Sebastian Hofferberth
2. Gutachter: Dr. Frank Vewinger

Contents

CHAPTER 1

Introduction

Frequency stabilizing lasers is useful in modern atomic physics experiments. Frequency stable lasers allow repeated measurements, where narrow atomic transitions are addressed, like atomic clocks [1], gravitational wave detection [2] and Rydberg atoms. In particular Rydberg atoms require narrow linewidth lasers to precisely drive an electron to the highly excited Rydberg state [3].

Rydberg states are often realized by alkali atoms such as Rubidium. Rubidium is commonly used in experiments with cold atoms that are often done with alkali-atoms [4]. One reason for the initial popularity of Rubidium for experiments with cold atoms was the convenient transition between the 5S ground state and the first excited state $5P_{3/2}$, which can be driven with 780 nm lasers [4]. Similar lasers were early on cheap and commonly available due to commercial applications like CD-Players [5]. The transitions from $5S_{1/2}$ to 6P can be driven by lasers in the visible frequency range. For example the $5S_{1/2}$ to $6P_{3/2}$ transition requires a laser at 420 nm. Together with a laser around 1012 nm, this transition can be used as the first step of a two photon excitation of Rubidium to its Rydberg state [6].

The work presented in this thesis was carried out in the context of the Rydberg Rubidium experiment in the nonlinear quantum optics group. The locking reference of the 780 nm lasers that are used for trapping and cooling Rubidium, is a ultra low expansion high finesse cavity. The cavity has a high finesse coating at different near infrared wavelengths. Due to the near infrared coating it is not possible to lock a 420 nm laser to the reference cavity. As an alternative we try to stabilize the 420 nm on a spectroscopic reference.

With a Toptica DL pro HP 420 we try to resolve the hyperfine states of the $6P_{3/2}$ excited state. This is done by sub-Doppler saturated absorption spectroscopy, where two counter propagating beams interact with the atomic Rb vapor [7]. One of the resulting Lamb peaks should be used as a stabilization reference.

There are multiple methods that use spectral features as a stabilization reference. There are e.g. polarization spectroscopy [8] or side of fringe locking [9]. In this thesis we use modulation transfer spectroscopy (MTS) [10]. In this method frequency sidebands are modulated by an electro optical modulator (EOM) to one of the beams. The sidebands are transferred via the nonlinear process of degenerate four wave mixing (DFWM) [11] to the other beam that is than used to create the error signal.

Earlier work on this setup was done by Sohn [12] in his bachelor thesis. In Section 2.2 we discuss the improvements made to previous versions of this setup to obtain higher absorption coefficients. This is followed by the characterization of the sub-Doppler spectrum Section 2.3 that is compared to work done by other research groups. The creation of the error signal together with the full MTS setup is described in Chapter 3.

CHAPTER 2

Saturated Absorption Spectroscopy of Rubidium $5S_{1/2}$ to $6P_{3/2}$ transitions

We want to stabilize a laser to a Rubidium spectroscopy feature for later driving the same transition as probe in the saturated spectroscopy. The two stable, naturally occurring Rubidium isotopes are ^{85}Rb with (72.17 ± 0.02) % and ^{87}Rb with (27.83 ± 0.02) % [13] [14]. In this chapter, we introduce the experimental setup to resolve the hyperfine transitions between the $5S_{1/2}$ ground state and $6P_{3/2}$ excited state in rubidium. We show how the beam waist and cell temperature enhances the signal to noise ratio in Doppler-broadened absorption spectroscopy. Lastly, we discuss how these experimental improvements increase the signal to noise ratio in sub-Doppler (saturated absorption) spectroscopy, that we later use to create an error signal.

2.1 Energy scheme of ^{85}Rb and ^{87}Rb

The nuclear angular momenta of the two natural isotopes are $I_{^{85}Rb} = 5/2$ and $I_{^{87}Rb} = 3/2$ [13] [16]. Rubidium is an alkali and therefore it has just one valence electron. The ground state has an angular momentum of $L = 0$ and spin of $S = 1/2$. According to LS - coupling the total angular momentum in the finestructure basis is $J = L + S = 1/2$ for both isotopes. Coupling this total angular momentum J with the total nuclear angular momenta I gives the total atomic angular momentum $F = J + I$ for each isotope. The magnitude of F can take values between $|J - I| \leq F \leq J + I$ that are non degenerate. This will split the ground state of ^{85}Rb into $F = 2$ and $F = 3$. Similar the ground state of ^{87}Rb is split into $F = 1$ and $F = 2$.

The laser that we are trying to lock is the Toptica DL pro HP 420 that operates around 420 nm $\approxeq$ 713.8 THz. Such that the used transition is $5S_{1/2}$ to $6P_{3/2}$. Fig. 2.1 shows the difference of frequency between those states. The excited state $6P_{3/2}$ has total angular momentum of $J = 3/2$. It couples with the total nuclear angular momenta to $F' = 1, 2, 3, 4$ for ^{85}Rb and $F' = 0, 1, 2, 3$ for ^{87}Rb. So in theory there will be 4 transitions from the ground state to the excited state (see blue arrows in Fig. 2.1) in the GHz range. Each of those transitions consist of 3 dipole allowed transitions between the hyperfine states that are in the MHz range. The GHz transitions can be resolved by absorption spectroscopy.

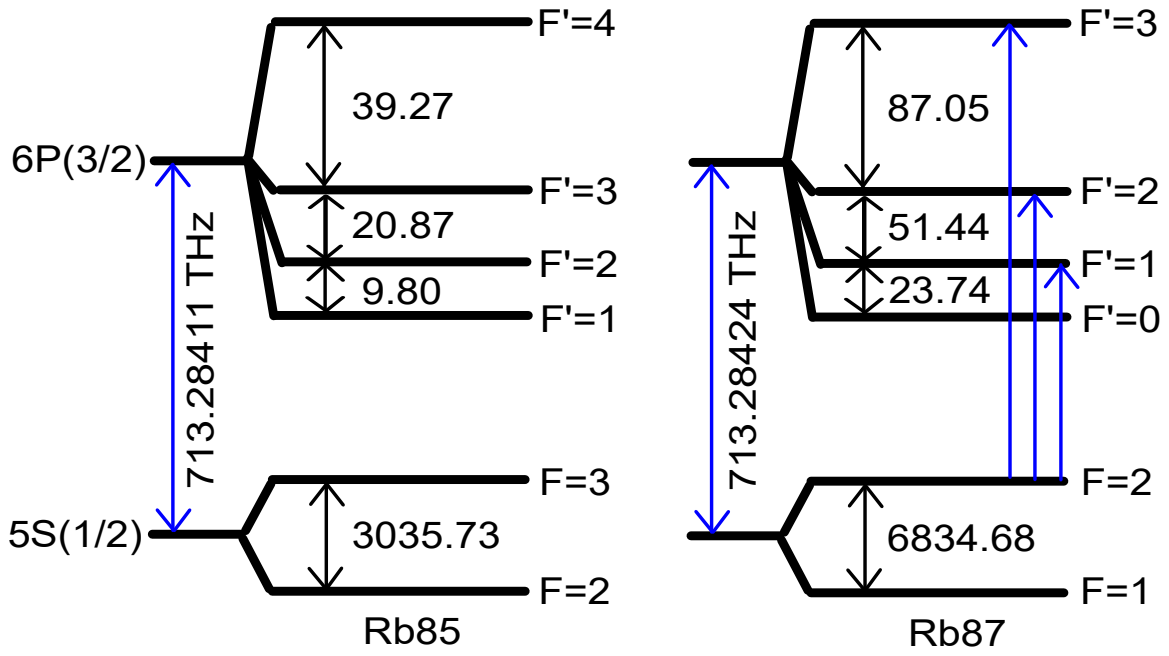

Figure 2.1: Level scheme and hyperfine splitting (rounded, in MHz) of the $5S_{\frac{1}{2}}$ and $6P_{\frac{3}{2}}$ state. The level splitting is not to scale and the values are taken from [15]. The blue arrows on the right show an example of the dipole allowed transitions for ^{87}Rb F = 2.

2.2 Absorption spectroscopy

Absorption spectroscopy is a often used method of measuring atomic transitions. A single collimated laser beam is propagating through a Rubidium vapor that absorbs light if the lasers frequency is on resonance with a atomic transition [17]. In a low temperature enviroment the lineshape of such an absorption is following the probability distribution given by the upper states lifetime. The absorption line has a Lorentzian shape. Due to the Rb vapor being heated to above $(100 \pm 1)\,^{\circ}$C, the atoms have a non zero velocity. The velocity for an ensemble of atoms follows the Maxwell-Boltzmann distribution, with in our case a mean velocity of 269 m/s. The velocity is calculated by the equilibrium of kinetic energy and thermal energy that is assumed here. If the atoms have a velocity component along the propagation axis of the laser beam, the beam will interact with different velocity classes of atoms. This is due to the Doppler effect. The Doppler effect causes a frequency detuning between the laser and the atomic transition frequency, such that the same transition ω of a moving atom is resonant with the laser at a different frequency ω' [17]

$$\omega' = \omega \pm k_z v_z \tag{2.1}$$

k_z is the wave vector of the light beam and v_z the velocity component of the atom along light propagation axis. With a non zero temperature of the vapor this effect is observable as a Gaussian shaped broadening, called Doppler broadening [17]. From the velocity calculated above we would obtain a broadening of roughly 650 MHz. The broadening limits the linewidth of a possible reference transition for frequency stabilization. To work in a sub-Doppler regime other methods like saturated absorption spectroscopy are used which is explained in Section 2.3.

2.2.1 Experimental setup

In Fig. 2.2 we show the setup to measure the absorption spectrum of Rubidium. The Laser is coupled

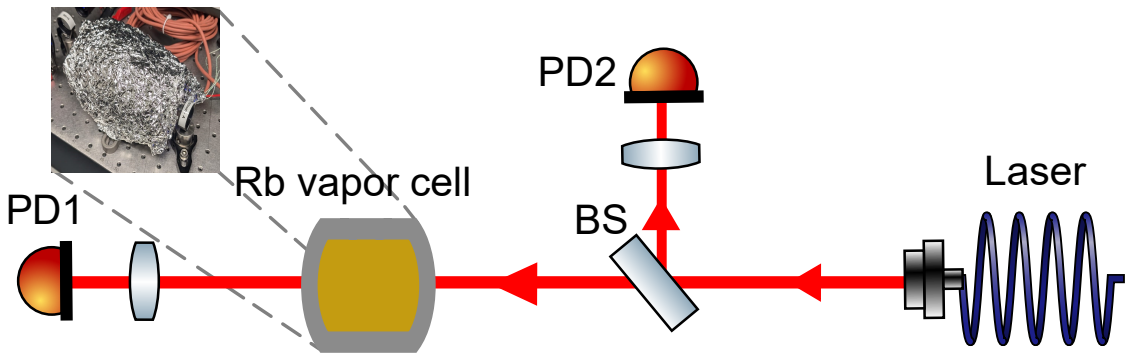

Figure 2.2: The laser beam is split by a beam splitter (BS). The transmission probes the Rb vapor cell and is detected by photodiode 1 (PD1). The vapor cell is embedded into a copper block (brown) and wrapped with aluminum (gray). The reflected portion is detected by photodiode 2 (PD2) and used as a reference.

into a single mode fiber to obtain a Gaussian shaped light beam. Than the beam is split on a 90/10 non-polarizing beam splitter (BS). The reflected low intensity part of the beam is detected by photodiode 2 (PD2). The signal is used as a reference to eliminate intensity changes arising from the laser frequency ramps. Photodiode 1 (PD1) detects the light that is transmitted trough the BS. The light transmitted through the BS is used for the spectroscopy. The beam behind the rubidium cell is detected with a second phototiode (PD1). The cell is embedded into a copper block that guarantees heating of the cell windows, such that the vapor does not condense. To increase the thermal isolation of the vapor cell it is wrapped in multiple layers of aluminum foil. In front of each photodiode is a lens that focuses the beam onto the photo sensitive chip. The cell is heated to above 100 °C. The heating is provided by heating cartridges that deliver in average 15 W of power. The detailed construction of the Rb vapor cell is described in Ref. [12].

2.2.2 Doppler broadened absorption spectrum

In previous attempts to create the frequency reference, the noise of the spectrum was on the same order as the actual reference signal amplitude [12]. This was suspected to be a result from a low absorption on resonance, due to the low scattering cross section of the $5S_{1/2}$ to $6P_{3/2}$ transition and the laser beam interacting with only a small number of atoms due to its finite size. Fig. 2.3 shows the Doppler broadened absorption spectrum at about (105 ± 1) °C. The absorption dips in the middle can easily be identified as the F = 3 and F = 2 to $6P_{3/2}$ transitions of ^{85}Rb. The outer dips correspond to the F = 2 (left) and F = 1 (right) to $6P_{3/2}$ transitions of ^{87}Rb. The calibrated transmission of the y-axis results from dividing the normalized signal of PD2, given by

$$I_{2,\text{norm}} = I_2 \cdot 10 \cdot (0.803 \pm 0.003) \cdot 0.1 + (7.9 \pm 0.1) \times 10^{-3}\text{mV} \tag{2.2}$$

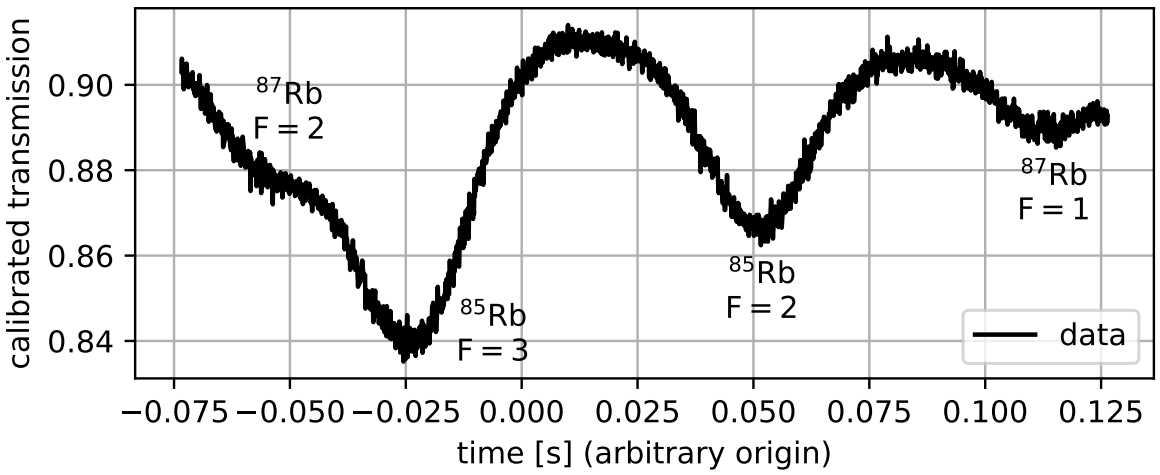

Figure 2.3: Doppler broadened spectroscopy of Rubidium around 420 nm. The outer left and outer right one correspond to the transitions of ^{87}Rb $5S_{1/2}$ F = 2 and F = 1 to $6P_{3/2}$. While the inner dips are due to the ^{85}Rb $5S_{1/2}$ F = 3 and F = 2 to $6P_{3/2}$ transitions. The calibration of the transmittance on the y-axis is explained in the main text.

With I_2 being the intensity measured by PD2 that is multiplied by 10, such that it matches the intensity of the probe light transmitted trough the non polarizing beam splitter. Furthermore the factor 0.803 ± 0.003 is due to reflections off the cell windows. Because a ND Filter of OD = 1.0 is placed in front of PD1, a factor of 0.1 contributes to the calibration. The added number at the end is the dark count offset of the PD which is different from PD1 with (6.6 ± 0.1) mV.

The amplitude of the ^{85}Rb F = 3 absorption dip relative to the off resonance offset of the spectrum is roughly (7.6 ± 0.3) %. The value is in agreement with relative absorption depth reached previously on the setup of also about 11 % [12]. As pointed out at the beginning of the chapter the noise of the measured spectrum reduces the accuracy of the reference transition. In this work we implement two upgrades to the setup to improve the absorption depth and by that enhancing the signal to noise ratio of the respective reference transitions amplitude.

2.2.3 Absorption spectroscopy with different beam waists

One improvement that easily can be implemented is increasing the size of the beam. Then the light is spread over a larger area such that it interacts with more atoms inside the vapor cell. To enlarge the beam, a telescope is placed between the vapor cell and the BS. We use the camera Arducam MT9J001 to determine the beam size. The beam is expected to have a Gaussian shape with $1/e^2$ radius w and mean value μ. The beam radius will be used as characteristic measure for the size. We extract the radius by fitting a Gaussian function to the data (shown in Fig. A.1)

$$I(x) = I_0 \exp\left(-\frac{2(x-\mu)^2}{w^2}\right) + \mathrm{C} \tag{2.3}$$

where I_0 is the peak intensity and C a constant offset. Comparing the fit parameters from the horizontal x-axis (Table A.1) with the ones from the vertical y-axis (Table A.2) reveals some asymmetry of the beam shape. In theory the beam should be a Gaussian mode due to exiting a polarization maintaining single mode fiber (PM-SMF) before reaching the spectroscopy setup. In reality the shape is influenced by imperfections of optical elements like from the beam splitter or a lens. Furthermore the Arducams orientation relative to the beam as well as the camera chip or filter itself could remove the Gaussian shape due to interference fringes. From collimation measurements performed without any optical elements the last two options seem to be reasonable arguments. Though the slight asymmetry of the beam will not limit out ability to perform spectroscopy with this beam.

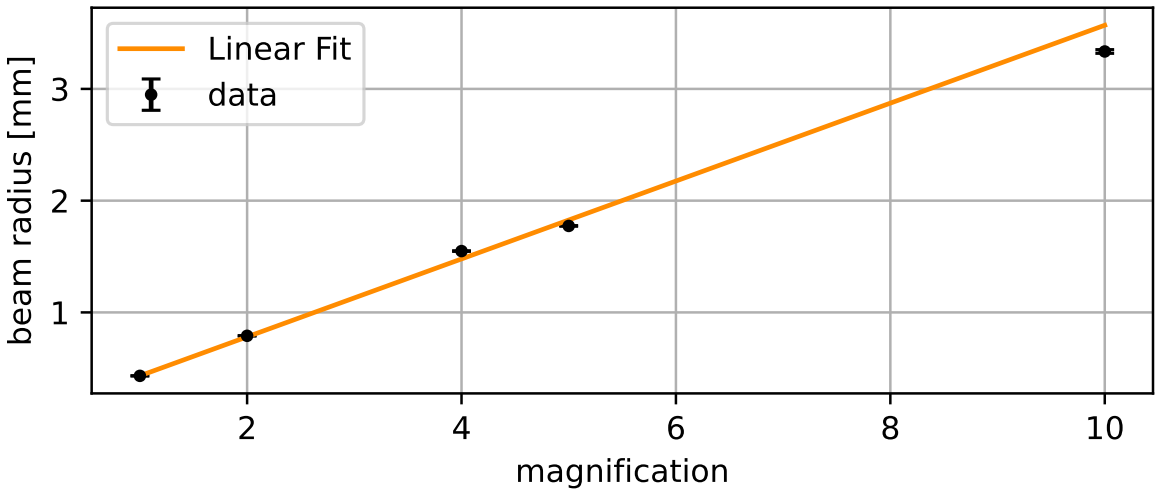

Figure 2.4: The plot displays a linear regression (orange) of the data on beam radius in relation to the magnification used. The fit quality is $\chi^2_{\text{red}} = 2.1$.

To calculate the rough beam size in future measurements it is useful to plot the relation between the measured beam radius and the magnification. The plot is shown in Fig. 2.4. The data points correspond to the average beam radius between the value for the x-axis and the value for the y-axis. The fit function used for the data is a linear function. That is due to the relation between the object O and the picture size P for a lens telescope with magnification $V = P/O$.

From the fit parameters, in Table A.3, we obtain the relation

$$w = (0.35 \pm 0.01)\,\text{mm} \cdot M + (0.08 \pm 0.01)\,\text{mm} \tag{2.4}$$

where M is the magnification factor. The errors of the fit are underestimated as also confirmed by $\chi^2_{\text{red}} = 2.1$. In this thesis a exact estimation of the beam radius is not needed, such that the fit is still good enough to work with it.

The effect of increasing the beam radius is shown by the oscilloscope images in Fig. 2.5. The important curve to observe in the images is the pink one which shows the ratio of the signal from PD1 (green) and PD2 (yellow). The images correspond to different magnifications, ranging from 1 to 4. We clearly observe increased absorption with enlarged beam radius. We observe an improved SNR as the noise on the photodiode does not increase with larger beam size. But there is a maximum beam radius due to the

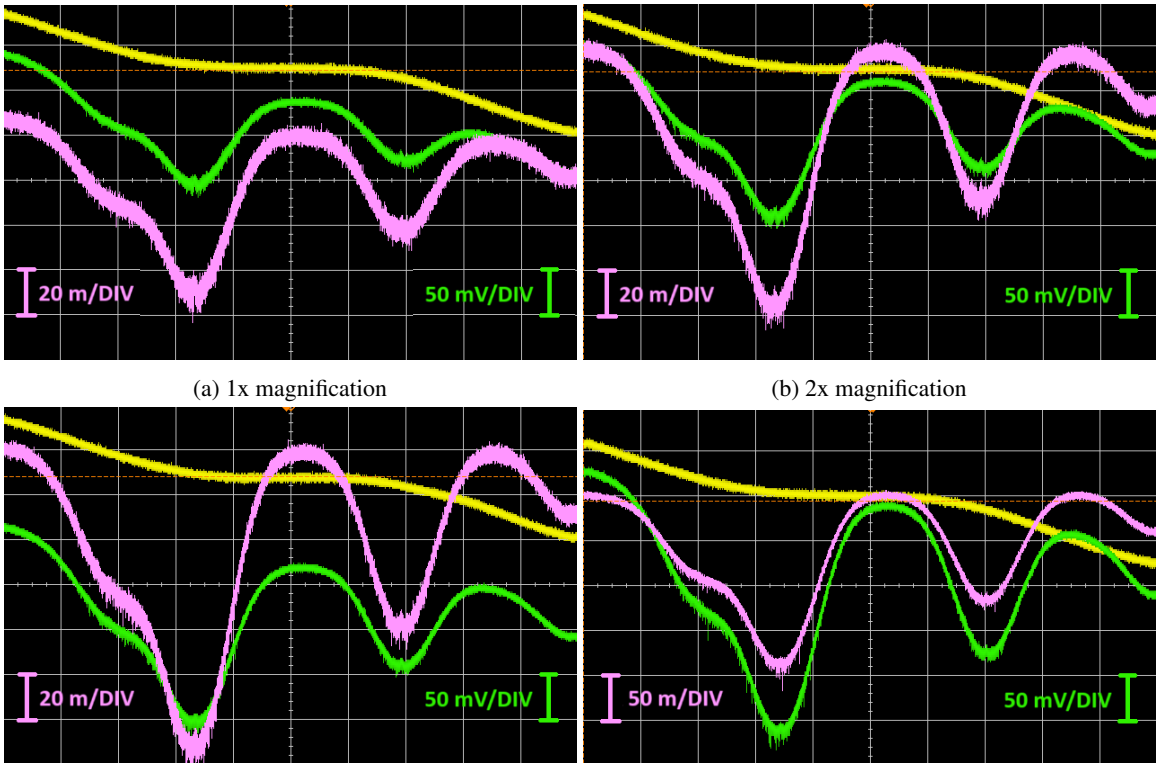

(a) 1x magnification

(b) 2x magnification

(c) 3x magnification

(d) 4x magnification

Figure 2.5: The oscilloscope images show the absorption signal on PD1 (green) at different magnifications of the beam. The reference signal of PD2 (yellow) as well as the normalized signal (pink) are shown too. While the PD signals have spacing of $V_{\mathrm{DIV,PD}} = 50\,\mathrm{mV/DIV}$, the normalized signal spacing is $V_{\mathrm{DIV,norm}} = 20\,\mathrm{mV/DIV}$ for 1x to 3x. While the 4x normalized signal is $V_{\mathrm{DIV,norm}} = 50\,\mathrm{mV/DIV}$

finite circular holes in the copper heating blocks, with a diameter of 10 mm.

2.2.4 Absorption spectroscopy with different temperatures

At room temperature the Rb $5S_{1/2}$ to $6P_{3/2}$ transition has a low scattering cross-section [18], compared to the $5S_{1/2}$ to $5P_{3/2}$ transition. So when using the first transition there is almost no visible absorption at room temperature. To counter this, the vapor cell is heated to over 100 °C (see Fig. 2.6(a)). With a rise in temperature the vapor pressure inside the cell will increase according to the relation given in [13][16]. A higher vapor pressure causes the atomic cloud to be more dense. This will cause more atoms to interact with the same beam intensity per unit area, compared to previous measurements. Sohn reached in his thesis a temperature slightly above 100 °C [12]. The idea is to further improve the isolation of the cell. When using the same voltage applied to the heating cartridges this should in principle result in a higher temperature. More isolation is in this work achieved by simply wrapping more layers of aluminum foil around the cell. For this measurement we use a magnification of 10x, corresponding to a averaged beam radius of $w = (3.33 \pm 0.02)$ mm.

It should be noted that the cell temperature is measured at the outer edge of the glass cell, such that the values do not fully represent the actual temperature of the Rb vapor, but it should be proportional.

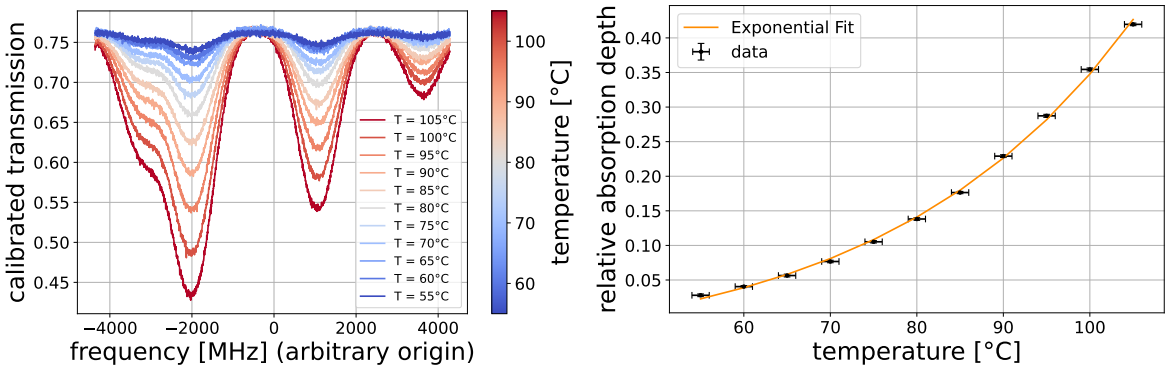

(a) (b)

Figure 2.6: (a) displays the absorption spectrum of the vapor cell for different temperatures. (b) is the fitted relation between relative absorption depth and cell temperature. The fit parameters can be found in Table A.4

Furthermore we noticed at the end that the measurement device was working on low battery which limited the accuracy of the temperature measurements for the following work of the thesis. Fig. 2.6(a) shows the evolution of the absorption spectrum with rising temperature. The different colors illustrate the temperature gradient. When comparing the temperature evolution spectrum to the Doppler broadened spectrum Fig. 2.3 it is apparent, that more light in general gets absorbed. While for the Doppler broadened spectrum there is (91 ± 1) % transmission, it significantly decreases to about (76 ± 1) % in the temperature gradient spectrum. This decrease in transmission is probably due to the increased beam size. With higher temperature there is additional broadening due to the Doppler broadening.

The absorption depth α increases exponentially with temperature T in $^{\circ}$C as it is expected from the logarithmic relation between the vapor pressure and the temperature inside the Rb cell [19]. Fig. 2.6(b) shows this exponential relation for the ^{85}Rb F = 3 transition with the fit parameters in Table A.4.

$$\alpha = 0.012 \pm 0.003 \cdot \exp(0.035 \pm 0.002 \cdot T) - 0.06 \pm 0.01 \tag{2.5}$$

From this model an increase of 15 to 20 $^{\circ}$C would result in nearly full absorption on resonance. Temperatures above (170 ± 1) $^{\circ}$C were reached. But with further increase of temperature the density of the Rb vapor increases which causes less transmission. With the additional Doppler broadening also due to increased temperature, the transmission of laser light trough the cell will drop to zero. To achieve large absorption depth, without losing too much transmission, the temperature is kept between (115 ± 1) $^{\circ}$C and (125 ± 1) $^{\circ}$C.

2.3 Saturated absorption spectroscopy

Locking a laser to the previously discussed Doppler broadened transitions would result in inaccurate stabilization. And in order to reach sub-Doppler linewidths with absorption spectroscopy, atoms need to be cooled down a lot [20]. A simpler way to achieve sub-Doppler linewidths is saturated absorption spectroscopy (SAS) [19]. Two counter propagating beams are overlapped inside the vapor cell. One beam, called the pump excites the atoms from the ground states to the excited state, assuming a two level system. The other beam probes this transition and is measured by a photodiode. The intensity of the pump is typically higher than that of the probe, such that the population in the ground and excited state equalizes.

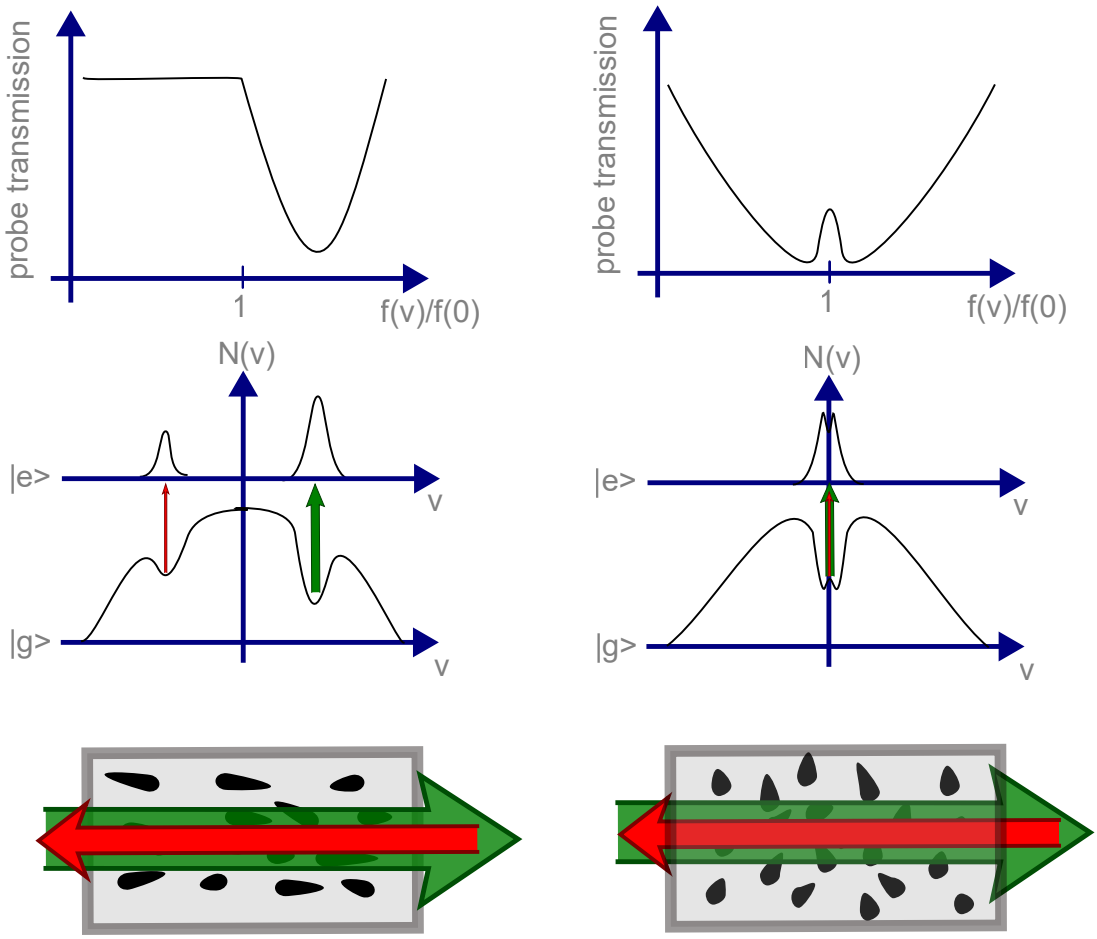

(a) (b)

Figure 2.7: (a) shows the off resonant case where probe (red) and pump (green) interact with atoms of different velocity classes, due to atoms moving along propagation. (b) shows the case for zero velocity

In the vapor cell the atoms are moving and most likely have a velocity component along the light propagation axis v_z. As explained in Section 2.2 this will cause a detuning between the atomic transition frequency and the laser. Because of the opposite propagation direction of probe and pump, they will

have opposite detuning relative to the transition frequency. Fig. 2.7(a) illustrates how the pump beam burns a hole into the ground state population of the moving atoms. The detuning of pump and probe causes them to interact with different atom classes, such that only absorption spectroscopy features are observed. If pump and probe interact with the same atoms, which is only the case when their v_z is equal to zero, the excited state population can undergo stimulated emission due to the probe being on resonance with the excited atoms as well. As a result the absorption reduces. A Lorentzian shaped peak will be visible in the absorption spectrum as illustrated in Fig. 2.7(b). Those peaks are called Lamb peaks and their width is on the order of the natural linewidth.

In reality other broadening effects need to be taken into account, when doing spectroscopy on sub-Doppler level, such as pressure and power broadening [21]. Pressure broadening occurs due to the higher vapor pressure caused by heating the cell [13][16]. Pressure broadening is in this experiment not really avoidable, because the cell needs to be heated. Power broadening occurs when the laser power exceeds the saturation intensity I_{sat}. The saturation intensity is given by [19]

$$I_{\text{sat}} = \frac{\pi}{3}\frac{hc}{\lambda^3 \tau} \tag{2.6}$$

where λ is the wavelength of the laser and τ is the lifetime of the excited state. The lifetime $\tau = (112.4 \pm 1.7)$ ns of the $6P_{3/2}$ state is taken from Ref. [22]. When reaching saturation, the absorption decreases on resonance more than off resonance. The changing absorption results in a broadened Voigt shaped peak, with a width $\Delta\omega_{\text{power}}$ [21]

$$\Delta\omega_{\text{power}} = \Gamma\left(1 + \frac{I}{I_{\text{sat}}}\right)^{\frac{1}{2}} \tag{2.7}$$

where I is the intensity of the laser beam. Such a Voigt curve is not easy to fit, because it is a convolution of a Gaussian and a Lorentzian. It will additionally limit the peak quality. So exceeding the saturation intensity should be avoided. Arising from Eq. (2.6) the saturation intensity of the $5S_{1/2}$ to $6P_{3/2}$ $\lambda = 420.27$ nm transition is $I_{\text{sat}} = (2.5 \pm 0.4)\ \frac{\text{mW}}{\text{cm}^2}$.

2.3.1 Experimental setup

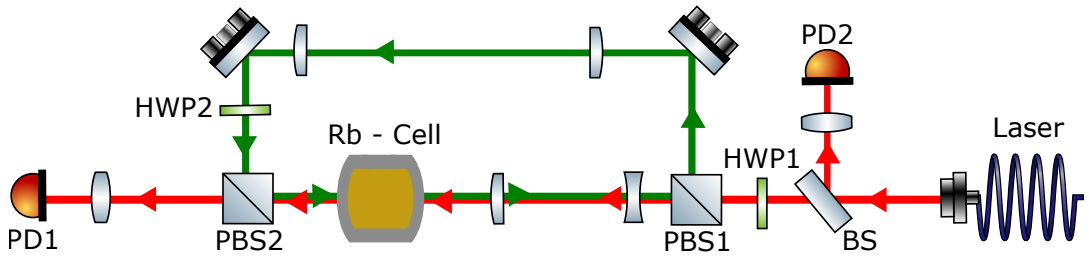

Figure 2.8: Experimental Setup of the SAS. The probe beam (red) is transmitted trough PBS1 and magnified. It is counter-propagating to and overlapped with the pump beam (green). HWP1 sets the pump/probe ratio for the two setups, while HWP2 and PBS2 are adjusting the amount of pump light going into the cell. The probe light is detected with PD1 and referenced to PD2.

Fig. 2.8 shows the experimental setup for SAS. The transmitted part of the polarization beam splitter (PBS) is the probe beam with a power of (1.4 ± 0.1) mW. The reflected beam (green) is the pump with a power of (4.1 ± 0.1) mW. So they are polarized orthogonal to each other. Their ratio is 3, but can be adjusted by turning HWP1. Both beams are magnified by telescopes with a magnification of 6. Derived from Eq. (2.4) the rough beam radius is $w = (0.218 \pm 0.006)$ cm. This will result in a saturation power of $P_{\text{sat}} = (0.37 \pm 0.06)$ mW. From Eq. (2.7) we expect a power broadening of $\Delta\omega_{\text{power}} = (3.1 \pm 0.5)$ MHz, due to the probe power used in the experiment. Then the pump is reflected by PBS2, such that it is counter-propagating relative to the probe. By adjusting the kinematic mirrors and PBS2 the beams are overlapped as much as possible. The pump intensity that is reaching the cell can be tuned by HWP2.

2.3.2 Characterization of the Lamb peaks

In the bachelor thesis previously written on spectroscopy of this laser, it was not possible to clearly resolve the Lamb peaks [12]. With the adjusted setup, described in Section 2.3.1 we achieved visible Lamp peaks without averaging the photodiode signal. The full spectrum is shown in Fig. 2.9. The

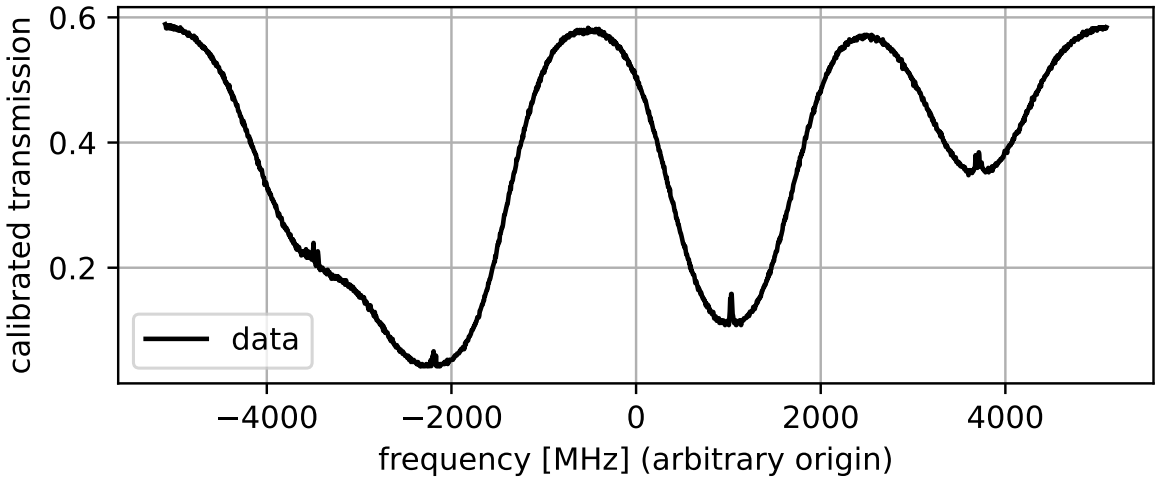

Figure 2.9: This Plot shows the Saturated absorption spectroscopy (Doppler-free) spectrum. It was measured with a cell temperature of $(120 \pm 5)\,^{\circ}$C.

splitting of the initial laser beam by PBS1 causes another factor of 0.33 to be multiplied to the y-axis calibration. The x-axis is calibrated by using the known frequency difference of two Doppler broadened dips. The calibration factor is $(204 \pm 3)\,\frac{\text{MHz}}{\text{ms}}$. In the spectrum the Lamb peaks are clearly visible and distinguishable from the noise.

From Fig. 2.10 the Lamb peaks of the dipole allowed transitions from each of the hyperfine ground states ($F_{85} = 2, 3$ and $F_{87} = 1, 2$) to the excited states ($F'_{85} = 1, 2, 3, 4$ and $F'_{87} = 0, 1, 2, 3$) can be identified. The three peaks left are due to cross-over (Co) resonances [21]. We now assume a 3-level system. Those cross-over peaks appear when the pump and the probe frequency is exactly halfway between two of the states. The beams now interact with the same two velocity classes of atoms. The pump for example can excite one class to the first excited state the other class to the second excited state. At the same time the probe does the opposite. This will leave a third peak exactly between the corresponding Lamb peaks. Due to the fact that the beams interact with two classes it is possible that

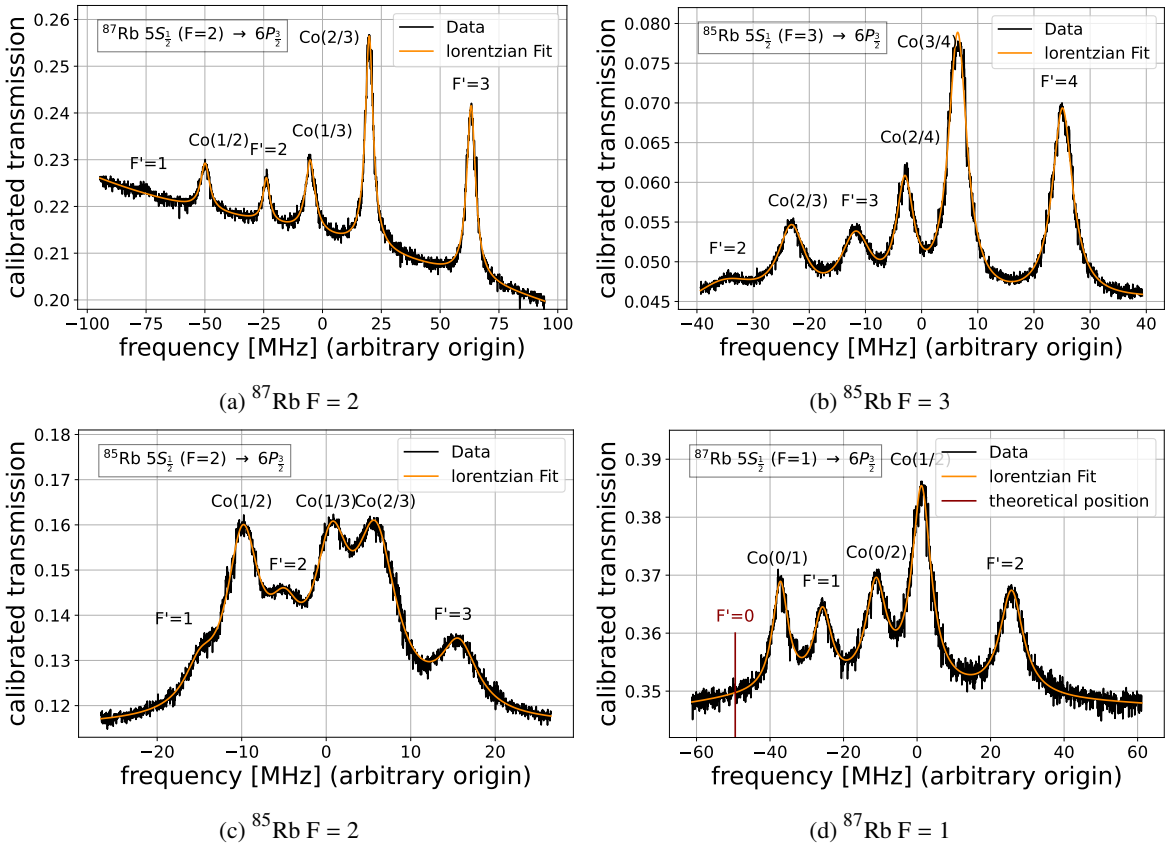

(a) ^{87}Rb F = 2

(b) ^{85}Rb F = 3

(c) ^{85}Rb F = 2

(d) ^{87}Rb F = 1

Figure 2.10: The plots display the SAS spectrum resulting from the hyperfine transitions between the ground states ($F_{85} = 2, 3$ and $F_{87} = 1, 2$) the excited states ($F'_{85} = 1, 2, 3, 4$ and $F'_{87} = 0, 1, 2, 3$). A superposition of six Lorentzian distributions are fit to the data.

cross-over peaks reach higher amplitudes than the Lamb peaks. However not every Lamp peak and crossover resonance is measured. For the ^{87}Rb $5S_{1/2}$ (F = 1) $6P_{3/2}$ it is not possible to identify the $F' = 0$ peak. Furthermore the $F' = 1$ peak of the ^{87}Rb $5S_{1/2}$ (F = 2) $\rightarrow$ $6P_{3/2}$ transition is not picked up by the fit function. It should be noted that the laser scan amplitude was changed to measure the different hyperfine transitions. That causes a different calibration of the x-axis for each of the four plots. This mentioned, the peaks resemble a Lorentzian shaped curve with amplitude $A_{0,i}$, peak center $x_{0,i}$ and full width at half maximum (FWHM) γ_i:

$$f\left(x_{0,i}, \gamma_i, A_{0,i}\right) = \sum_{i=1}^{6} A_{0,i} \frac{\gamma_i^2}{\left(x_i - x_{0,i}\right)^2 + \gamma_i^2} + mv + b \tag{2.8}$$

The additional linear offset is due to the fact that the Lorentzian shaped peaks sit on top of the Doppler broadened dips and are not always perfectly centered in a minimum. The parameters of the fit are written in Table A.5 - A.8.

A comparison of the data with theoretical values is done by calculating the frequency difference for each transition in the $6P_{3/2}$ manifold. Table 2.1 shows mostly agreement between experimental and

Table 2.1: Hyperfine splitting of the Rb $6P_{\frac{3}{2}}$ state

	Transition	$\Delta\nu_{0,\text{measured}}$ [MHz]	Literature [MHz]
^{85}Rb $6P_{\frac{3}{2}}$	$F' = 1 \leftrightarrow F' = 2$	10.00 ± 0.05	9.80
	$F' = 2 \leftrightarrow F' = 3$	20.66 ± 0.03, 23.3 ± 0.2	20.85
	$F' = 3 \leftrightarrow F' = 4$	36.81 ± 0.04	39.27
^{87}Rb $6P_{\frac{3}{2}}$	$F' = 0 \leftrightarrow F' = 1$		23.74
	$F' = 1 \leftrightarrow F' = 2$	59 ± 7, (51.42 ± 0.03)	51.45
	$F' = 2 \leftrightarrow F' = 3$	(87.05 ± 0.05)	87.05

theoretical data of the ^{85}Rb $6P_{3/2}$ splitting. The exception is the second value of the $F' = 2 \leftrightarrow F' = 3$ transition, where the value deviates from the other transitions. Closely looking at the corresponding fit in Fig. 2.10(b) one can point out a small difference between the fit and the data shaping the $F' = 2$ peak. In the data of ^{87}Rb the bracketed values are the transitions used for calibrating each of the two spectra. Which means those are not valid for discussion of the data quality. In addition the $F' = 1$ peak cannot be identified, but it's theoretical position calculated from the other peak positions is marked in Fig. 2.10(d). The large deviation and error results from the peak being identified by the fit at a wrong position.

In saturated absorption spectroscopy the Lamb and crossover peaks are expected to have a Lorentzian shape due to the linewidth being on the order of the natural linewidth, as long as $I_{\text{pump/probe}} \ll I_{\text{sat}}$. If the Intensity exceeds the saturation limit it will cause power broadening that gives a peak in the form of a Voigt profile [19]. In average the measured linewidth (see Table A.5 - A.8) (FWHM) $\approxeq (2.58 \pm 0.03)$ MHz is nearly twice as large as it is to be expected from the natural linewidth 1.416MHz [15]. In reality other broadening effects need to be taken into account, such as power and pressure broadening [17]. The measured linewidth is roughly in agreement with what is to be expected from the power broadening calculated in Section 2.3.1 of $\Delta\omega_{\text{power}} = (3.1 \pm 0.5)$ MHz. Still there is a deviation that is probably due to the calculation being not as precise. The linewidth could be improved by using crossover free spectroscopy techniques [23]. Alternatively the power of the probe can be adjusted to reduce power broadening or a decrease of temperature in the vapor cell could decrease vapor pressure.

Compared to previous work done with MTS [10] [15] the linewidth is on the same order of magnitude (2 - 3MHz), such that it should not limit the SNR of the error signals.

CHAPTER 3

Modulation Transfer Spectroscopy

In the earlier sections of this thesis a high resolution spectroscopy signal is described. The sub-Doppler peaks are narrow enough to be used as stabilization reference. In this thesis we use modulation transfer spectroscopy (MTS) which has the advantage of creating a dispersive signal with near zero noise background. The zero crossing of this signal is centered on the atomic resonance [10]. The idea behind MTS is that frequency sidebands are modulated onto the pump beam. Through the process of degenerate four wave mixing (DFWM), the sidebands will be transferred onto the probe. The transfer only happens when probe and pump are interacting with atoms of velocity zero which also is the advantage to other modulation spectroscopy methods.

3.1 Electro optical modulator

The modulation of frequency sidebands is done in this thesis by electro optical modulation (EOM). The working principle of the EOM is based on the Pockels effect [24]. The Pockels effect describes the change of the refractive index in a birefringent crystal, caused by an applied electric field. We use a Lithium niobate ($LiNbO_3$) crystal. It has two refractive indices, the ordinary n_o and the extraordinary n_e. Applying the electric field now along one of those axes, changes the corresponding refractive index, depending on electric field direction and polarization of the light. We choose the electric field and the polarization of the light to be parallel along the extraordinary axis. The change of the extraordinary refractive index Δn_e is determined by [25]:

$$\Delta n_e(t) = -\frac{n_e^3}{2} r_{33} E_3(t) \tag{3.1}$$

where r_{33} is one of the electro optical (EO) coefficients. It describes the case of the linear polarization and the direction of modulating electric field $E_3(t)$ pointing in the direction of the extraordinary axis. With $r_{33} = 30.8 \times 10^{-12}$ m/V ($LiNbO_3$) [24] being about 3.5 times larger then the EO coefficient of the orientation along the ordinary axis, the change of refractive index requires a lower modulation amplitude. This change, results in a new extraordinary refractive index n_e'

$$n_e' = n_e + \Delta n_e(t). \tag{3.2}$$

that will modulate a phase shift onto the pump beam as described in the following equation:

$$\Phi(t) = -\frac{2\pi\Delta n_e(t)L}{\lambda_0} = \frac{\pi n_e^3 r_{33} L}{\lambda_0} E_3(t) \tag{3.3}$$

where λ_0 is the vacuum wavelength of the pump beam and L the length of the crystal. The voltage to achieve a phase shift of π is denoted by V_π and is used to characterize the modulation efficiency of an EOM. By considering two capacitor plates on either side of the extraordinary axis an electric field of $E = \frac{V}{d}$ can be assumed, where V is the applied voltage and d the distance between the plates. Putting this into Equation Eq. (3.3) gives

$$V_\pi = \frac{\lambda_0 d}{-n_e^3 r_{33} L}. \tag{3.4}$$

Placing the crystal in an electric resonance circuit improves V_π. In this setup the EOM has a resonance frequency of (3.533 ± 0.001) MHz. Further information on the construction of the EOM is provided in [12].

The pump beam, under the assumption of a monochromatic plane wave, is in general described by [26]

$$E_{\text{pump}}(t) = E_0 \cos(\omega t + \Phi(t)) \tag{3.5}$$

where E_0 is the maximum electrical field amplitude of the pump with an optical frequency ω. The modulation of the pump causes a time dependend phase shift $\Phi(t)$. A sinosodial modulation $\Phi(t) = M \sin(\omega_{\text{m}} t)$ with modulation index M and frequency ω_{m} generates frequency sidebands that follow the upcoming equation

$$E_{\text{pump}}(t) = E_0 \sum_k J_{\text{k}}(M) \cos((\omega + k\omega_{\text{m}})t). \tag{3.6}$$

Here $J_{\text{k}}(M)$ is the Bessel-function of first order that is determining the sidebands intensity. In addition k is the number of sidebands with $k \gg M$ being negligible in this thesis [26].

3.2 Pockels cell

We verify the functionality of the EOM by performing a Pockels cell measurement. In a Pockels cell the EOM is placed after a HWP (see Fig. 3.1) that turns a linear polarized light beam 45° relative to the extraordinary axis of the EOMs crystal. The EOM sits on the focal point of the Kepler telescope that ensures a homogeneous modulation of the light beam. With such a setup the EOM modulates the phase shift between the vertical and the horizontal polarization component. By placing a PBS after the EOM, the intensity of the transmitted horizontal component of the light will be observed. HWP3 turns the linear polarization of the pump and the transmission of PBS2 is detected by PD3. Due to the PBS, the intensity will change according to Malus' law as shown in Fig. 3.2. As measured earlier for this setup by Sohn [12], the modulation voltage of 8 V_{pp} corresponds to a phase modulation of roughly $0.6 \cdot 2\pi$. Also the transmission drops from about 520 mV to roughly 0 mV which is optimal for a clear modulation. The DC offset of the minimum in the signal indicates that the light is not fully polarized.

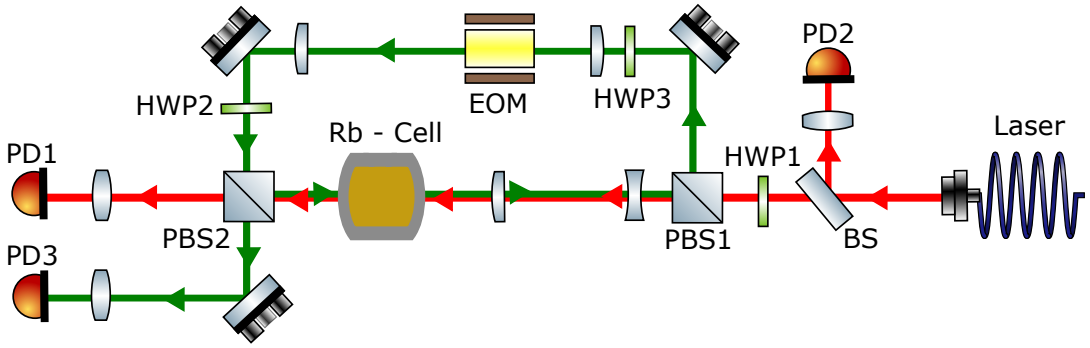

Figure 3.1: Setup of the Pockels cell measurement. PD3 detects the polarization changes that are induced to the modulation of the EOM. HWP3 is used to adjust the polarization relative to the modulating axis of the EOMs crystal.

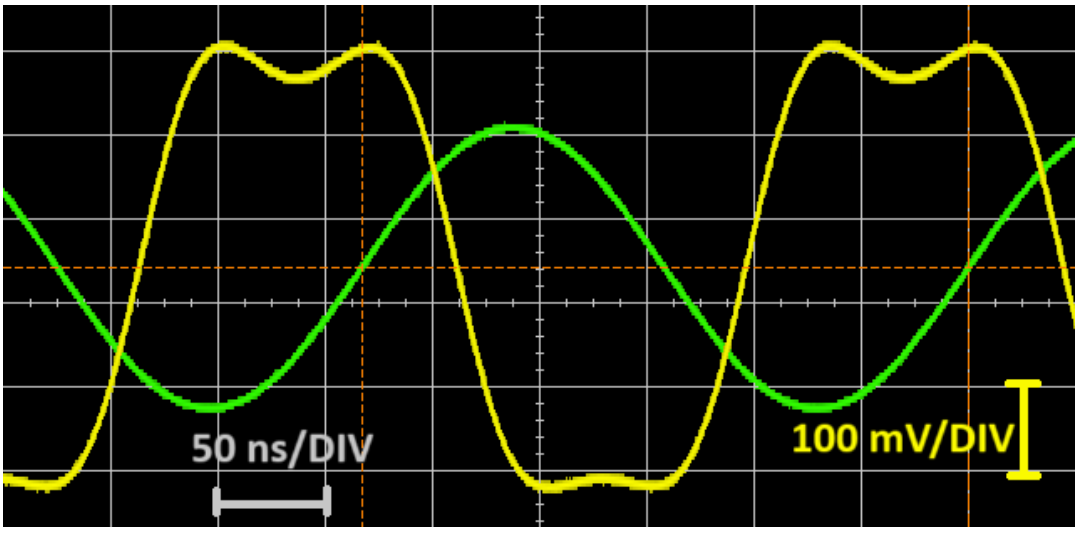

Figure 3.2: Oscilloscope image of the Pockels cell measurement. Channel 1 (yellow) displays the signal from PD3. The modulation signal given to the EOM is shown on channel 2 (green).

3.3 Creation of the error signal

Modulation transfer occurs when two frequency components of the pump, e.g. the carrier and a sideband, interact with the probe through degenerate four wave mixing (DFWM) [11] to create a fourth wave, a sideband for the probe. DFWM is a consequence of the third order non-linear susceptibility component of the Rb vapor. In the case of strong susceptibility, a fourth wave corresponding to a probe sideband is created. Due to the modulation transfer being purely nonlinear, the MTS signal is insensitive to background absorption in the medium [27]. The probe and its sidebands are detected by PD1, as shown in Fig. 3.3. Arising from DFWM the RF photodiode signal will consist of an in-phase term that is proportional to the Doppler-free peaks and a quadrature term that is proportional to the dispersion [28]. A dual channel signal generator drives the EOM with its resonance frequency of 3.533 MHz to modulate the pump beam. The other channel of the signal generator gives the local oscillator (LO) signal with

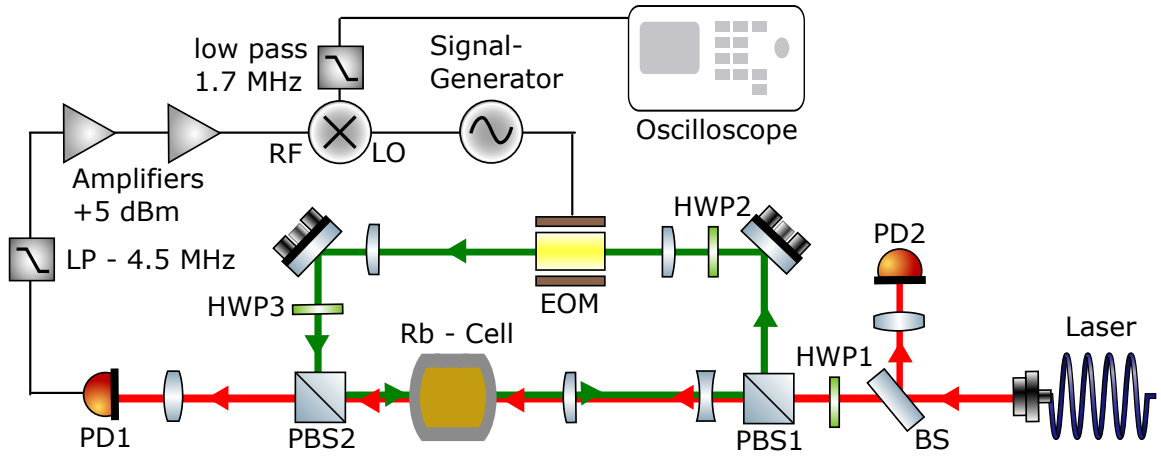

Figure 3.3: A EOM is added to the SAS setup to modulate the pump (green). The PD1 output signal is DC blocked, because only AC components are needed. To get a clear signal it is amplified by two amplifiers and used as one input of a mixer. While the other component of the mixer is a Local oscillator with the modulation frequency of 3.5 MHz. Then the mixed signal is fed trough a low pass filter to eliminate unwanted frequency components into the oscilloscope.

the same frequency as the modulation to demodulate the RF signal with a mixer after passing trough a 4.5 MHz low pass filter and two amplifiers. The amplitude of the LO signal is set to $1.416\,\mathrm{V_{pp}}$ due to the properties of LO input of the mixer (ZFL-500LN+). For the lossless ideal mixer the output has a fast oscillating term with the sum of the two input frequencies and a term that only depends on the phase ϕ between the PD signal and the local oscillator:

$$\cos(\omega_\mathrm{M} t + \phi)\cos(\omega_\mathrm{M} t) = \frac{1}{2}\left(\cos(\phi) + \cos(2\omega_\mathrm{M} t + \phi)\right) \tag{3.7}$$

Because the fast oscillating term from Eq. (3.7) disturbs the error signal, it is cut off by a 1.7 MHz low pass filter. So the remaining output is a DC signal that depends only on the phase between the RF signal and the LO signal. We adjust the phase of the LO with the signal generator, such that there is a relative phase shift to the RF signal.

3.4 Analysis of the error signals

Fig. 3.4 shows spectral features (violet) together with the corresponding demodulated signal (black). A 10 point moving is applied to the data for visualization (orange). For this measurement the modulation depth is set to $M = 6\,\mathrm{V_{pp}}$. The total beam power coming out of the fiber is (7.2 ± 0.1) mW. The probe power is set to (0.49 ± 0.01) mW and the pump power to (2.7 ± 0.2) mW. The y-axis of the probe transmission is shifted to an arbitrary origin. The x-axis is calibrated by the known frequency difference of the lamb peaks and is the same for all the following measurements.

In Fig. 3.4(a) we observe dispersion features with zero crossings at the center frequency of the corresponding spectral features. It is also apparent that the error signal of the $\mathrm{F}' = 4$ peak is the largest. This results from the degenerate four wave mixing being most efficient for closed transitions, like the

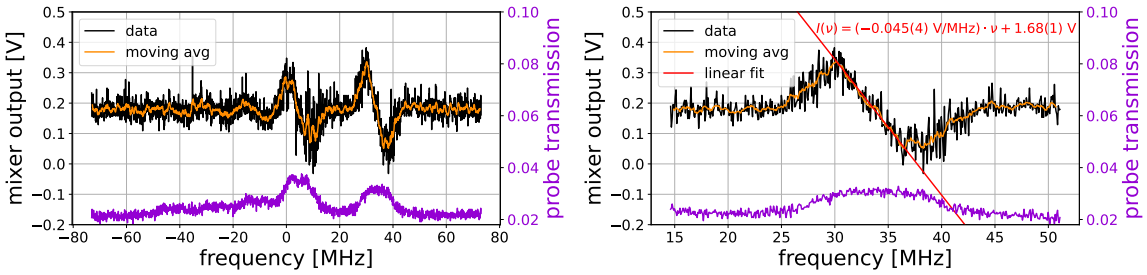

(a) Manifold of the ^{85}Rb $5S_{1/2}$ F = 3 to $6P_{3/2}$

(b) ^{85}Rb $5S_{1/2}$ F = 3 to $6P_{3/2}$ F′ = 4

Figure 3.4: Plot (a) shows the error signal of the ^{85}Rb $5S_{1/2}$ F = 3 to $6P_{3/2}$ transitions (black) with the corresponding Doppler-free spectrum (violet). Plot (b) is just displaying the F′ = 4 features. A 10 point moving average is applied to both plots. The red curves resembles the linear fit to the error signals slope.

^{85}Rb $5S_{1/2}$ F = 3 to $6P_{3/2}$ F′ = 4. So even if the spectral feature of the cross-over peak is larger that does not mean that the error signal is as well.

The dispersion shape of the error signals arises from scanning the laser through the transitions. When locking the laser we will not scan it, so the error signal will be a DC signal that depends on the frequency of the laser relative to one of the zero crossings. With an ideal mixer we would expect the error signal to have no DC component. Still we observe a offset of about 0.2 V in Fig. 3.4. This offset probably results from intensity noise components that are independent of the spectral feature. In upcoming measurements the DC offset will be set to zero.

To reliably stabilize a laser a maximum peak to peak amplitude as well as a steep gradient at the zero crossing is required. From this argument we choose the F′ = 4 peak as a reference to create the error signal which is shown in more detail in Fig. 3.4(b). By fitting a linear function to the slope of the error signal (red line in the plot) we obtain a slope of (-0.045 ± 0.004) V/MHz. This value is in agreement with the observations made by Ref. [10] and [26] at a modulation frequency of 3.5 MHz. In this chapter we show how the error signal can be optimized by adjusting the phase, the RF modulation amplitude and the probe to pump beam power ratio.

Phase variation

By changing the phase of the LO it is possible to determine if the demodulation of the RF signal is working, because the error signal should be depending on the phase shift between RF and LO signal Eq. (3.7). In Fig. 3.5 the saturated absorption spectrum (violet) and the corresponding error signal (black) is displayed. The spectrum is normalized to an arbitrary origin such that changes are comparable. To simplify the calculations and visualize the changes in the signal a 20 point moving average (orange) is calculated for the demodulation signal. For this measurements we use a modulation amplitude of $M = 6\,\mathrm{V_{pp}}$. At the cell we measure a probe power of (0.49 ± 0.01) mW and a pump power of (2.7 ± 0.2) mW. The phase is decreased for with each plot from left to right and top to bottom by -45°. Starting with a phase of 15° at the top left and ending at -345° in the bottom right. In total a phase shift of 360° is applied. We can clearly observe changes in the shape of the error signal when changing the phase. Signals with a relative phase of 180° are antisymmetric to each other as it is to be expected from Eq. (3.7).

Fig. 3.6 shows the fit of a sin-function, with the fit parameters in Table A.10. The peak to peak

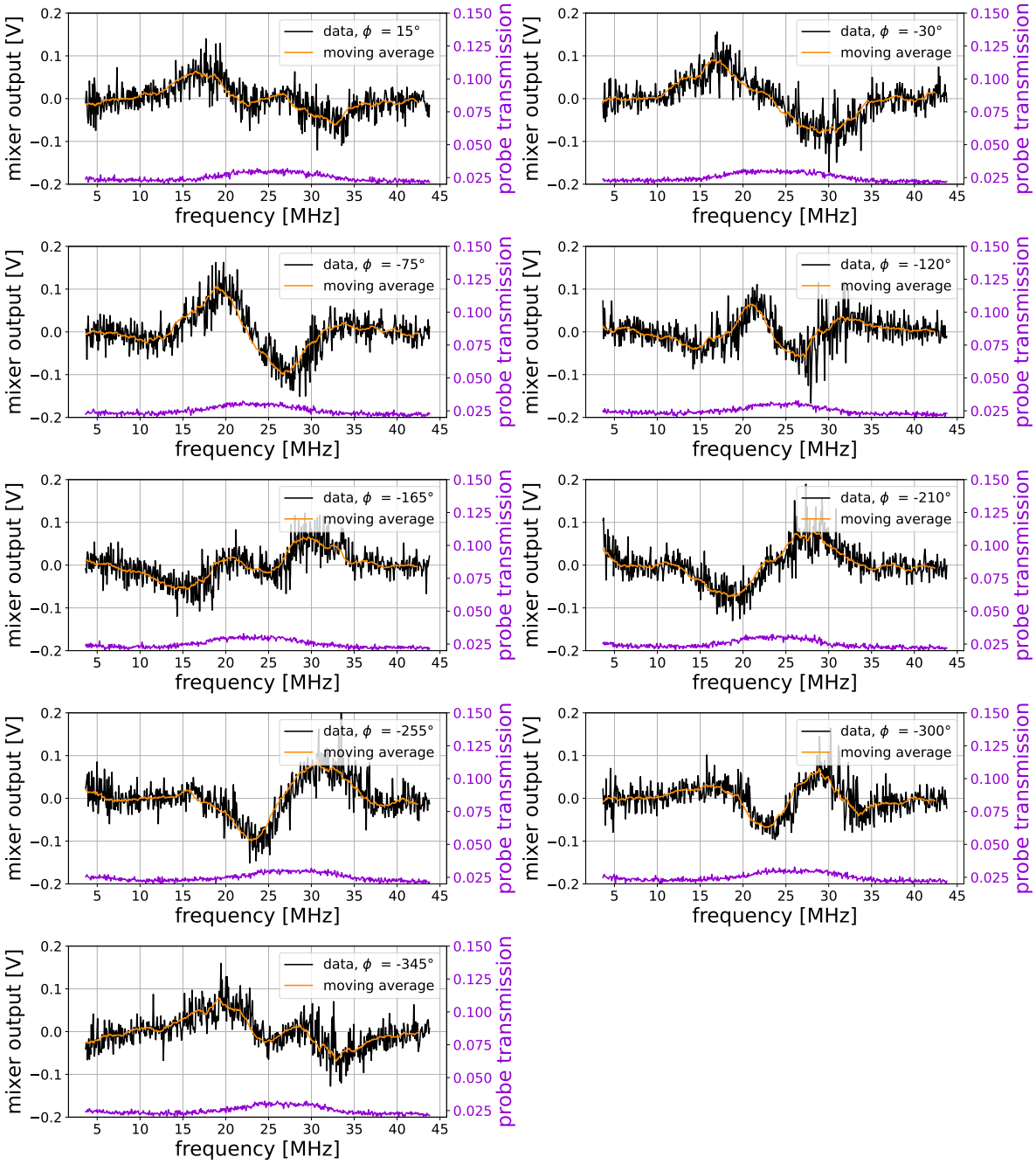

Figure 3.5: The single plots contain the measured photodiode signal (violet) and the error signal (black). Additionally a 20 point moving average (orange) is applied to the data. The 5 x 2 plot grid resembles the deformation of the demodulated signal with a change of phase. The phase decreases by 45° from left to right and up to down. For comparability of the signal shapes all signals where shifted to 0 V DC-offset.

amplitude is modified by sign, depending on the sign of the slope. The fit indicates a sinusoidal correlation between the modified peak to peak amplitude of the error signal and the phase. Still there

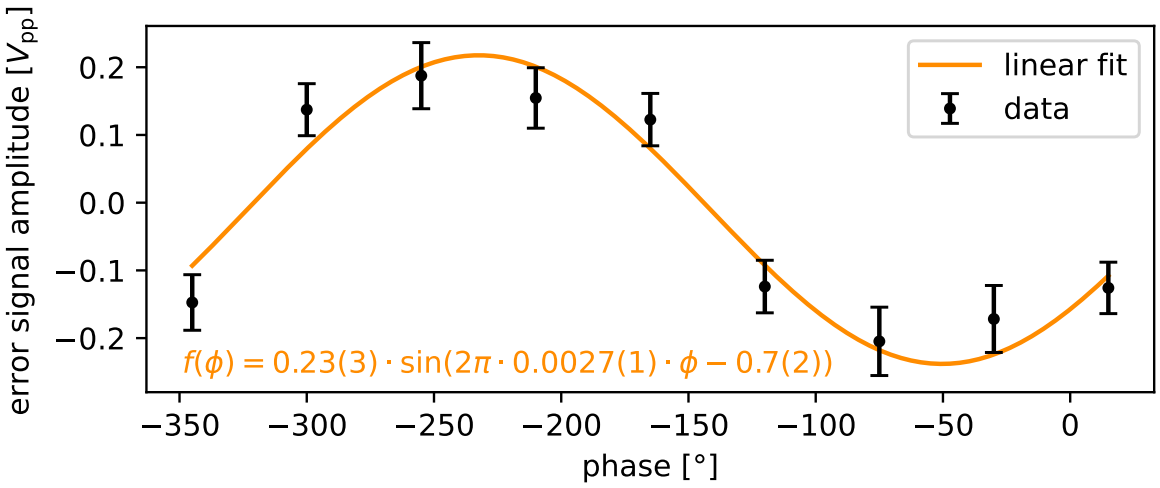

Figure 3.6: The plot shows the evolution of the error signal peak to peak amplitude with a change of phase. The data with corresponding RMS error is shown by the black points with error bars. A sinusoidal fit is displayed in orange

are large errors due the root mean square (RMS) noise in the signal that limits the accuracy of this measurement. We can conclude that the phase should be tuned for each set of parameters, such that we obtain a maximum peak to peak amplitude. In this measurement a suitable error signal is created by the phases 75° and 255°.

Modulation amplitude

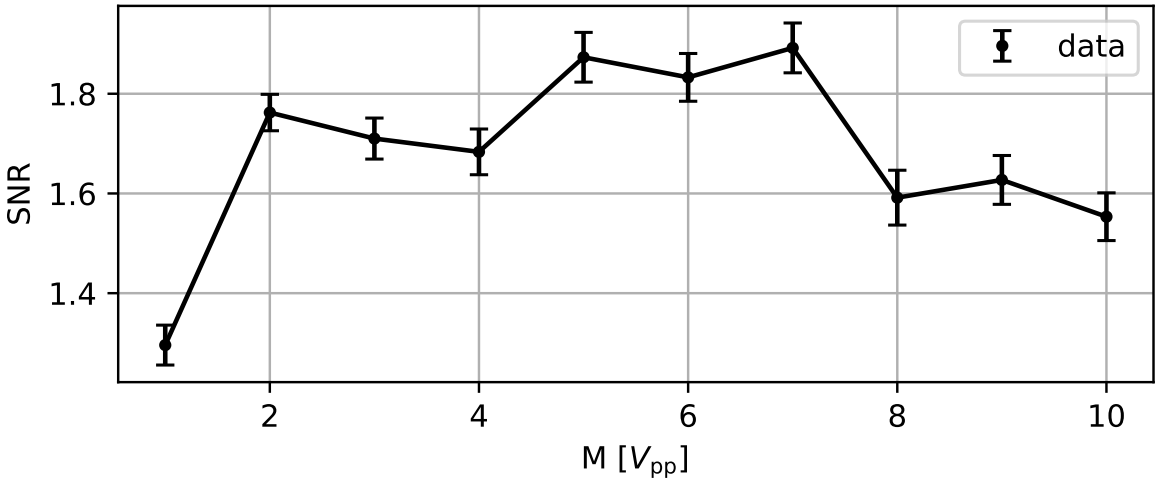

Figure 3.7: The plot presents the peak to peak amplitude of the error signal with respect to the modulation depth applied to the EOM.

In Fig. 3.7 we present the influence of the modulation depth on the Signal to noise ratio of the error

signal. The SNR is calculated by

$$\mathrm{SNR} = \frac{\text{Amplitude } \left[\mathrm{V_{pp}}\right]}{2 \cdot \mathrm{RMS } \left[\mathrm{V_{pp}}\right]} \tag{3.8}$$

The peak to peak amplitude is taken from the data in Fig. A.2. From the plot we obtain a maximum SNR at $M = (6 \pm 1)\,\mathrm{V_{PP}}$. For higher modulation depth the peak to peak amplitude of the error signal drops. This can be explained by a splitting of the Lamb peak that is observed with increased modulation. The splitting results from a bigger portion of light that is modulated onto the frequency sidebands of the probe instead of the carrier. This causes the absorption to increase slightly on atomic resonance ω_0, and decrease at $\omega_0 \pm \omega_\mathrm{m}$. Resulting from the splitting the error signal will also split, causing a decrease of the peak to peak amplitude. This is further explained in [10].

Beam ratio

Another parameter that influences the accuracy of the error signal is the power ratio of the probe and the pump beam. While changing the ratio in this measurement, the modulation depth is constant at $M = 6\,\mathrm{V_{pp}}$ and the phase is set to $-64°$. The error signal amplitudes in Fig. 3.8 decrease with lower

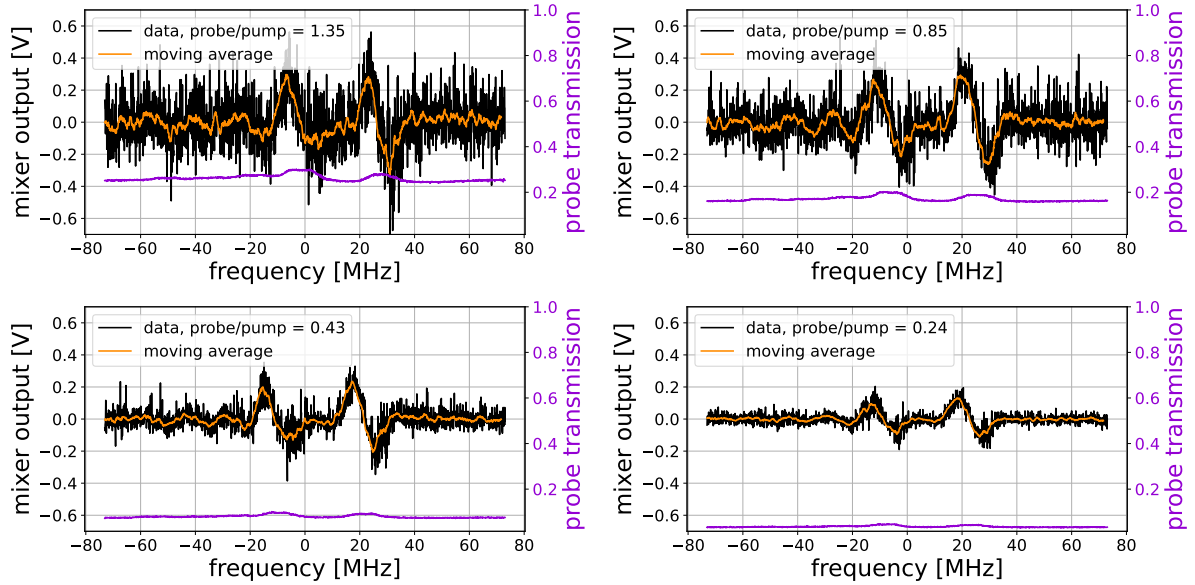

Figure 3.8: The figure presents the spectrum with corresponding error signals for different probe to pump power ratios. The ratio increases from left to right and top to bottom.

probe power. This arises from less probe light probing the excited state atoms, such that there is also less nonlinear interaction between the pump and the probe. Less interaction means then weaker sidebands on the probe, resulting in a decreased error signal amplitude. A higher probe to pump ratio seems to increase the noise of the error signal. By increasing the probe power more light is detected on the photodiode. This will increase the Lamp peaks as well as the noise, which will leave the SNR of the spectrum unchanged. But the modulation remains the same, because it is not affected by the probe power. Due to additionally amplifying the noise, the SNR of the error signal decreases. The plots indicate that probe and pump power should be set carefully, because it changes the quality of the error signal.

Due to a lack of data and time constraints it was not possible to give a value for the optimal probe to pump power ratio. But from the data that was taken it is suspected to be roughly 0.50(25). Additionally changing the overall laser power could be investigated in the future, to reduce the linewidth resulting from power-broadening. A narrower linewidth should in principle result in a steeper slope of the error signal [26].

Demodulation bandwidth

One has to choose the low pass filter after the mixer for the required application. A lower cut off frequency gets rid of high frequency noise (as shown in Fig. 3.9), but also limits the bandwidth within the laser can be frequency stabilized. This means that for a small frequency low pass, fast changes of

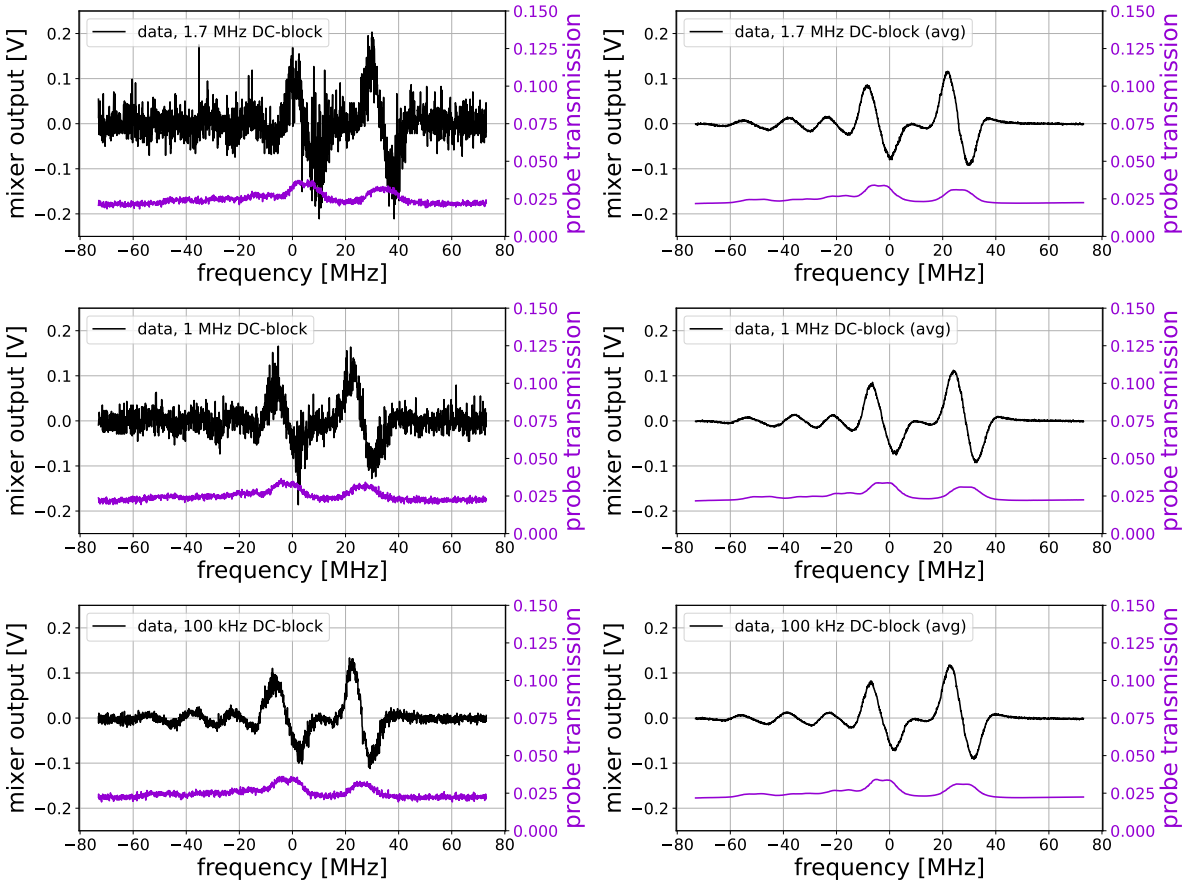

Figure 3.9: In the left column are the error signals for different DC-Blocks at the mixers output. The right column displays a 8 point average on the oscilloscope

the laser frequency cannot be measured. Typically a bandwidth of 1 to 2 MHz is used, as it is the usual range for laser locking. With a modulation frequency of $\omega_m = 3.533$ MHz we were able to create an error signal with a signal to noise ratio of 1.83 ± 0.05. This error signal has a averaged peak to peak amplitude of $(0.18 \pm 0.05)\ V_{pp}$. Due to time constraints it was not possible to measure the error signal for different modulation frequencies. From Ref. [10] and [26] we know that there should be an optimal

modulation frequency that still need to be determined for this setup.

CHAPTER 4

Conclusion

The aim of this thesis was to create an error signal for locking a 420 nm laser to the $5S_{1/2}$ to $6P_{3/2}$ transition of Rubidium. The error signal was created with modulation transfer spectroscopy, where sidebands are modulated onto the pump beam of a saturated absorption spectroscopy setup. The modulation of the pump beam is transferred onto the probe beam if they are resonant with the same atoms in the Rubidium vapor cell. To generate a usable error signal it is therefore necessary to have a significant absorption through the rubidium vapor, which required multiple adjustments compared to previous works [12].

First of all, the beams for the SAS were enlarged with telescopes, which increased the signal to noise ratio of the absorption. To further maximize the absorption the vapor cell isolation was improved by more aluminum foil wrapped around the cell. Instead of about 100 °C in earlier attempts, we reached temperatures of more than 130 °C. With the larger beams and a temperature between 115 and 125 °C an absorption depth of 100 % could be reached. The in average measured linewidth of $\cong (2.58 \pm 0.03)$ MHz of the spectral features are nearly twice as wide as the natural linewidth. This is in agreement with other works where linewidths of 2 to 3 MHz were measured.

With the improved SAS it was possible to create the desired error signal with a signal to noise ratio of 1.83 ± 0.05. It was shown that the error signals shape depends periodically on the phase as it is to be expected from the demodulation process. We determined that for a given modulation frequency ω_m the modulation depth M and the phase Φ need to be adjusted in order to obtain a error signal with a steep slope and a large peak to peak amplitude.

Despite from reaching the error signal there is still room for improvements. First of all adjusting the total beam power could decrease the linewidth of the Lamb peaks and additionally increase the slope of the error signal.

Secondly, by changing the inductance of the EOM resonance circuit it is possible to adjust the EOMs resonance frequency. Other research groups showed that the error signal quality is different depending on the chosen modulation frequency [10]. So similar measurements should be done to further increase the quality of the error signal. Also the polarization of the beams can contribute to the error signal, which should be investigated.

Lastly if the parameters M, Φ, probe to pump power, total power and polarization are optimized it is possible to use a PID controller to setup the feedback circuit for the laser stabilization. This will also need further optimization.

Is all this done the laser can be coupled into a fiber and used in the main experiment to drive the two photon Rubidium Rydberg excitation.

CHAPTER 5

Acknowledgements

I would like to thank Sebastian Hofferberth for the opportunity to write my thesis in his group. I also thank Frank Vewinger for being my second examiner. Thank you to the nonlinear quantum optics group for making me feel welcome. I am very glad that Lukas Ahlheit and Nina Stiesdal were my supervisors. So special thanks for their continuous support and help. Their expertise was an important part for the success of this thesis. Also thanks to Simon Schroers and Daniil Svirskiy for the additional support. Thanks to my lab partner Jeremy Binda who helped me staying motivated in the time span of this thesis. Thanks to the persons that, additionally to persons mentioned above, proofread my thesis, Delia Siedenberg and Felix Becker. Finally i would like to thank my family and Luisa Frohnapfel for supporting me through this project.

Bibliography

[1] N. Hinkley et al. "An Atomic Clock with 10^{-18} Instability". In: *Science* 341.6151 (2013), pp. 1215–1218. DOI: 10.1126/science.1240420. eprint: https://www.science.org/doi/pdf/10.1126/science.1240420. URL: https://www.science.org/doi/abs/10.1126/science.1240420 (cit. on p. 1).

[2] B P Abbott et al. "LIGO: the Laser Interferometer Gravitational-Wave Observatory". In: *Reports on Progress in Physics* 72.7 (2009), p. 076901. DOI: 10.1088/0034-4885/72/7/076901. URL: https://dx.doi.org/10.1088/0034-4885/72/7/076901 (cit. on p. 1).

[3] Thomas Gallagher. "Rydberg Atoms". In: *Springer Handbook of Atomic, Molecular, and Optical Physics*. Ed. by Gordon Drake. New York, NY: Springer New York, 2006, pp. 235–245. ISBN: 978-0-387-26308-3. DOI: 10.1007/978-0-387-26308-3_14. URL: https://doi.org/10.1007/978-0-387-26308-3_14 (cit. on p. 1).

[4] Robert Löw et al. "An experimental and theoretical guide to strongly interacting Rydberg gases". In: *Journal of Physics B: Atomic, Molecular and Optical Physics* 45.11 (2012), p. 113001. DOI: 10.1088/0953-4075/45/11/113001. URL: https://dx.doi.org/10.1088/0953-4075/45/11/113001 (cit. on p. 1).

[5] T. C. Bakker Schut et al. "Optical-trapping micromanipulation using 780-nm diode lasers". In: *Opt. Lett.* 18.6 (1993), pp. 447–449. DOI: 10.1364/OL.18.000447. URL: https://opg.optica.org/ol/abstract.cfm?URI=ol-18-6-447 (cit. on p. 1).

[6] E. Brekke and C. Umland. "Rydberg excitation through detuned microwave transition in rubidium". In: *J. Opt. Soc. Am. B* 40.11 (2023), pp. 2758–2761. DOI: 10.1364/JOSAB.502442. URL: https://opg.optica.org/josab/abstract.cfm?URI=josab-40-11-2758 (cit. on p. 1).

[7] Wolfgang Demtröder. *Laser Spectroscopy 2: Experimental Techniques*. Springer Berlin, Heidelberg, 2015. ISBN: 978-3-662-44641-6 (cit. on p. 1).

[8] T.W. Hansch and B. Couillaud. "Laser frequency stabilization by polarization spectroscopy of a reflecting reference cavity". In: *Optics Communications* 35.3 (1980), pp. 441–444. ISSN: 0030-4018. DOI: https://doi.org/10.1016/0030-4018(80)90069-3. URL: https://www.sciencedirect.com/science/article/pii/0030401880900693 (cit. on p. 1).

[9] R. L. Barger, M.S. Sorem and J.L. Hall. "Frequency stabilization of a cw dye laser". In: *Applied Physics Letters* 22.11 (June 1973), pp. 573–575. ISSN: 0003-6951. DOI: 10.1063/1.1654513. eprint: https://pubs.aip.org/aip/apl/article-pdf/22/11/573/18427741/573_1_online.pdf. URL: https://doi.org/10.1063/1.1654513 (cit. on p. 1).

[10] D J McCarron, S A King and S L Cornish. "Modulation transfer spectroscopy in atomic rubidium". In: *Measurement Science and Technology* 19.10 (Aug. 2008), p. 105601. ISSN: 1361-6501. DOI: 10.1088/0957-0233/19/10/105601. URL: http://dx.doi.org/10.1088/0957-0233/19/10/105601 (cit. on pp. 1, 13, 14, 18, 21, 22, 24).

[11] R. K. Raj et al. "High-Frequency Optically Heterodyned Saturation Spectroscopy Via Resonant Degenerate Four-Wave Mixing". In: *Phys. Rev. Lett.* 44 (19 1980), pp. 1251–1254. DOI: 10.1103/PhysRevLett.44.1251. URL: https://link.aps.org/doi/10.1103/PhysRevLett.44.1251 (cit. on pp. 1, 16).

[12] Bennet Sohn. "Creation of Error Signals for Frequency-stabilizing a Grating Laser to Rubidium Transitions Using Modulation Transfer Spectroscopy". Bachelor Thesis. Universität Bonn, 2024. URL: https://www.nqo.uni-bonn.de/publications/publications/2024-bennet-sohn-bachelor.pdf (cit. on pp. 1, 4, 5, 7, 11, 15, 24).

[13] Daniel A. Steck. *Rubidium 85 D Line Data,'* URL: http://steck.us/alkalidata (visited on 23/01/2025) (cit. on pp. 2, 7, 10).

[14] E. J. Catanzaro et al. "Absolute Isotopic Abundance Ratio and Atomic Weight of Terrestrial Rubidium". In: *Journal of Research of the National Bureau of Standards. Section A, Physics and Chemistry* 73A.5 (1969), pp. 511–516. DOI: 10.6028/jres.073A.041 (cit. on p. 2).

[15] Conny Glaser et al. "Absolute frequency measurement of rubidium $5S-6P$ transitions". In: *Phys. Rev. A* 102 (1 2020), p. 012804. DOI: 10.1103/PhysRevA.102.012804. URL: https://link.aps.org/doi/10.1103/PhysRevA.102.012804 (cit. on pp. 3, 13).

[16] Daniel A. Steck. *Rubidium 87 D Line Data,'* URL: http://steck.us/alkalidata (visited on 23/01/2025) (cit. on pp. 2, 7, 10).

[17] Wolfgang Demtröder. *Laser Spectroscopy 1: Basic Principles*. Springer Berlin, Heidelberg, 2014. ISBN: 978-3-642-53859-9 (cit. on pp. 3, 13).

[18] C. D. Herold et al. "Precision Measurement of Transition Matrix Elements via Light Shift Cancellation". In: *Phys. Rev. Lett.* 109 (24 2012), p. 243003. DOI: 10.1103/PhysRevLett.109.243003. URL: https://link.aps.org/doi/10.1103/PhysRevLett.109.243003 (cit. on p. 7).

[19] Daniel A. Steck. *Quantum and Atom Optics*. 2024. URL: http://steck.us/teaching (cit. on pp. 8–10, 13).

[20] Alexander Dunning et al. "Interferometric Laser Cooling of Atomic Rubidium". In: *Phys. Rev. Lett.* 115 (7 2015), p. 073004. DOI: 10.1103/PhysRevLett.115.073004. URL: https://link.aps.org/doi/10.1103/PhysRevLett.115.073004 (cit. on p. 9).

[21] C.J. Foot. *Atomphysik*. Oldenbourg Wissenschaftsverlag GmbH, 2011. ISBN: 978-3-486-70546-1 (cit. on pp. 10, 11).

[22] M. S. Safronova and U. I. Safronova. "Critically evaluated theoretical energies, lifetimes, hyperfine constants, and multipole polarizabilities in ^{87}Rb". In: *Phys. Rev. A* 83 (5 2011), p. 052508. DOI: 10.1103/PhysRevA.83.052508. URL: https://link.aps.org/doi/10.1103/PhysRevA.83.052508 (cit. on p. 10).

[23] Ayan Banerjee and Vasant Natarajan. “Saturated-absorption spectroscopy: eliminating crossover resonances by use of copropagating beams”. In: *Opt. Lett.* 28.20 (2003), pp. 1912–1914. DOI: 10.1364/OL.28.001912. URL: https://opg.optica.org/ol/abstract.cfm?URI=ol-28-20-1912 (cit. on p. 13).

[24] R. S. Weis and T. K. Gaylord. “Lithium niobate: Summary of physical properties and crystal structure”. In: *Applied Physics A* 37.4 (1985), pp. 191–203. ISSN: 1432-0630. DOI: 10.1007/BF00614817. URL: https://doi.org/10.1007/BF00614817 (cit. on p. 14).

[25] Pochi Yeh Amnon Yariv. *Optical Waves in Crystals: Propagation and Control of Laser Radiation*. Wiley, 2002. ISBN: 978-0-471-43081-0 (cit. on p. 14).

[26] Tilman Preuschoff, Malte Schlosser and Gerhard Birkl. “Optimization strategies for modulation transfer spectroscopy applied to laser stabilization”. In: *Optics Express* 26.18 (Aug. 2018), p. 24010. ISSN: 1094-4087. DOI: 10.1364/oe.26.024010. URL: http://dx.doi.org/10.1364/OE.26.024010 (cit. on pp. 15, 18, 22).

[27] Jing Zhang et al. “Characteristics of absorption and dispersion for rubidium D2 lines with the modulation transfer spectrum”. In: *Opt. Express* 11.11 (2003), pp. 1338–1344. DOI: 10.1364/OE.11.001338. URL: https://opg.optica.org/oe/abstract.cfm?URI=oe-11-11-1338 (cit. on p. 16).

[28] Gary C. Bjorklund. “Frequency-modulation spectroscopy: a new method for measuring weak absorptions and dispersions”. In: *Opt. Lett.* 5.1 (1980), pp. 15–17. DOI: 10.1364/OL.5.000015. URL: https://opg.optica.org/ol/abstract.cfm?URI=ol-5-1-15 (cit. on p. 16).

APPENDIX A

Appendix

A Tables

Table A.1: fit parameters of arducam measurements in x-direction

magnification	I_0 [no unit]	μ [mm]	w [mm]	C [no unit]
1x	28455 ± 16	1.56 ± 0.00	0.4273 ± 0.0003	36470 ± 4
2x	60206 ± 121	2.45 ± 0.00	0.7718 ± 0.0019	37245 ± 49
4x	76357 ± 122	2.51 ± 0.00	1.4583 ± 0.0034	44352 ± 99
5x	111796 ± 113	2 ± 0.00	1.6620 ± 0.0025	55874 ± 109
10x	231754 ± 2874	2.08 ± 0.00	3.6228 ± 0.0324	36190 ± 2953

Table A.2: fit parameters of arducam measurements in y-direction

magnification	I_0 [no unit]	μ [mm]	w [mm]	C [no unit]
1x	27947 ± 18	3.67 ± 0.00	0.4372 ± 0.0003	27363 ± 4
2x	58785 ± 88	3.32 ± 0.00	0.8093 ± 0.0015	27730 ± 29
4x	78558 ± 136	2.98 ± 0.00	1.6393 ± 0.0039	29667 ± 89
5x	110908 ± 191	2.98 ± 0.00	1.8858 ± 0.0047	36978 ± 151
10x	173083 ± 297	3.40 ± 0.00	3.0470 ± 0.0060	60706 ± 322

Table A.3: fit parameters of the linear fit to obtain a relation between beam size and magnification

m [mm]	b [mm]
0.35 ± 0.01	0.08 ± 0.01

Table A.4: fit parameters of Fig. 2.6

['p_0']	['p_1']	['p_2']
0.0120 ± 0.0026	0.0353 ± 0.0019	−0.0606 ± 0.0124

Table A.5: fit parameters of 87Rb (F=2)

$\nu_{0,i}$ [MHz]	γ_i [MHz]	a_i
-83 ± 7	81 ± 18	$(-0.7 \pm 0.2) \times 10^{-3}$
-49.89 ± 0.06	2.26 ± 0.09	$(0.98 \pm 0.02) \times 10^{-2}$
-23.88 ± 0.05	-1.71 ± 0.08	$(0.94 \pm 0.03) \times 10^{-2}$
-5.24 ± 0.04	2.44 ± 0.06	$(1.53 \pm 0.02) \times 10^{-2}$
19.87 ± 0.01	2.04 ± 0.02	$(4.54 \pm 0.02) \times 10^{-2}$
63.17 ± 0.01	2.26 ± 0.02	$(3.70 \pm 0.02) \times 10^{-2}$
m [1/MHz]	b_i	
-0.00017 ± 0.00001	0.217 ± 0.002	

Table A.6: fit parameters of 85Rb (F=3)

$\nu_{0,i}$ [MHz]	γ_i [MHz]	a_i
-35.1 ± 0.2	7.8 ± 0.7	$(0.42 \pm 0.03) \times 10^{-2}$
-23.16 ± 0.04	2.96 ± 0.09	$(0.93 \pm 0.02) \times 10^{-2}$
-11.73 ± 0.04	3.4 ± 0.1	$(0.83 \pm 0.02) \times 10^{-2}$
-2.98 ± 0.02	1.88 ± 0.03	$(1.40 \pm 0.01) \times 10^{-2}$
6.424 ± 0.008	2.01 ± 0.02	$(3.35 \pm 0.01) \times 10^{-2}$
25.08 ± 0.01	2.20 ± 0.02	$(2.41 \pm 0.01) \times 10^{-2}$
m [1/MHz]	b_i	
0.000032 ± 0.000005	0.0438 ± 0.0001	

Table A.7: fit parameters of 85Rb (F=2)

$\nu_{0,i}$ [MHz]	γ_i [MHz]	a_i
-14.97 ± 0.06	2.2 ± 0.1	$(8.1 \pm 0.2) \times 10^{-3}$
-9.86 ± 0.02	2.38 ± 0.04	$(3.74 \pm 0.03) \times 10^{-2}$
-4.96 ± 0.04	2.4 ± 0.1	$(1.50 \pm 0.03) \times 10^{-2}$
0.62 ± 0.02	2.52 ± 0.05	$(3.17 \pm 0.03) \times 10^{-2}$
5.87 ± 0.02	2.95 ± 0.03	$(3.68 \pm 0.03) \times 10^{-2}$
15.69 ± 0.04	2.67 ± 0.06	$(1.49 \pm 0.02) \times 10^{-2}$
m [1/MHz]	b_i	
0.000005 ± 0.000003	0.11542 ± 0.00009	

Table A.8: fit parameters of 87Rb (F=1)

$\nu_{0,i}$ [MHz]	γ_i [MHz]	a_i
-73 ± 39	-27 ± 23	$(-4 \pm 5) \times 10^{-3}$
-37.21 ± 0.03	2.56 ± 0.08	$(1.85 \pm 0.02) \times 10^{-2}$
-25.71 ± 0.05	2.99 ± 0.11	$(1.30 \pm 0.02) \times 10^{-2}$
-11.17 ± 0.04	3.38 ± 0.08	$(1.75 \pm 0.02) \times 10^{-2}$
1.19 ± 0.02	3.16 ± 0.04	$(3.46 \pm 0.02) \times 10^{-2}$
25.71 ± 0.04	3.84 ± 0.08	$(1.81 \pm 0.01) \times 10^{-2}$
m [1/MHz]	b_i	
-0.00003 ± 0.00001	0.349 ± 0.001	

Table A.9: Peak to peak amplitudes for different modulations. The phase was tuned to maximum peak to peak amplitude

M [V_{pp}]	A_{pp} [V_{pp}]	Φ [°]
1	0.10 ± 0.04	245
2	0.13 ± 0.04	277
3	0.14 ± 0.04	122
4	0.15 ± 0.05	116
5	0.19 ± 0.05	130
6	0.18 ± 0.05	146
7	0.19 ± 0.05	117
8	0.18 ± 0.06	126
9	0.16 ± 0.05	124
10	0.15 ± 0.05	127

Table A.10: Peak to peak amplitudes for different phases.

Φ [°]	A_{pp} [V_{pp}]
15	0.13 ± 0.03
-30	0.17 ± 0.04
-75	0.20 ± 0.05
-120	0.12 ± 0.03
-165	0.12 ± 0.04
-210	0.15 ± 0.04
-255	0.19 ± 0.04
-300	0.14 ± 0.03
-345	0.15 ± 0.04

Table A.11: Peak to peak amplitudes for different probe to pump ratios.

probe/pump	A_{pp} $\left[V_{pp}\right]$
1.35 ± 0.02	0.62 ± 0.17
0.85 ± 0.02	0.56 ± 0.15
0.43 ± 0.02	0.44 ± 0.10
0.24 ± 0.02	0.24 ± 0.06

B Figures

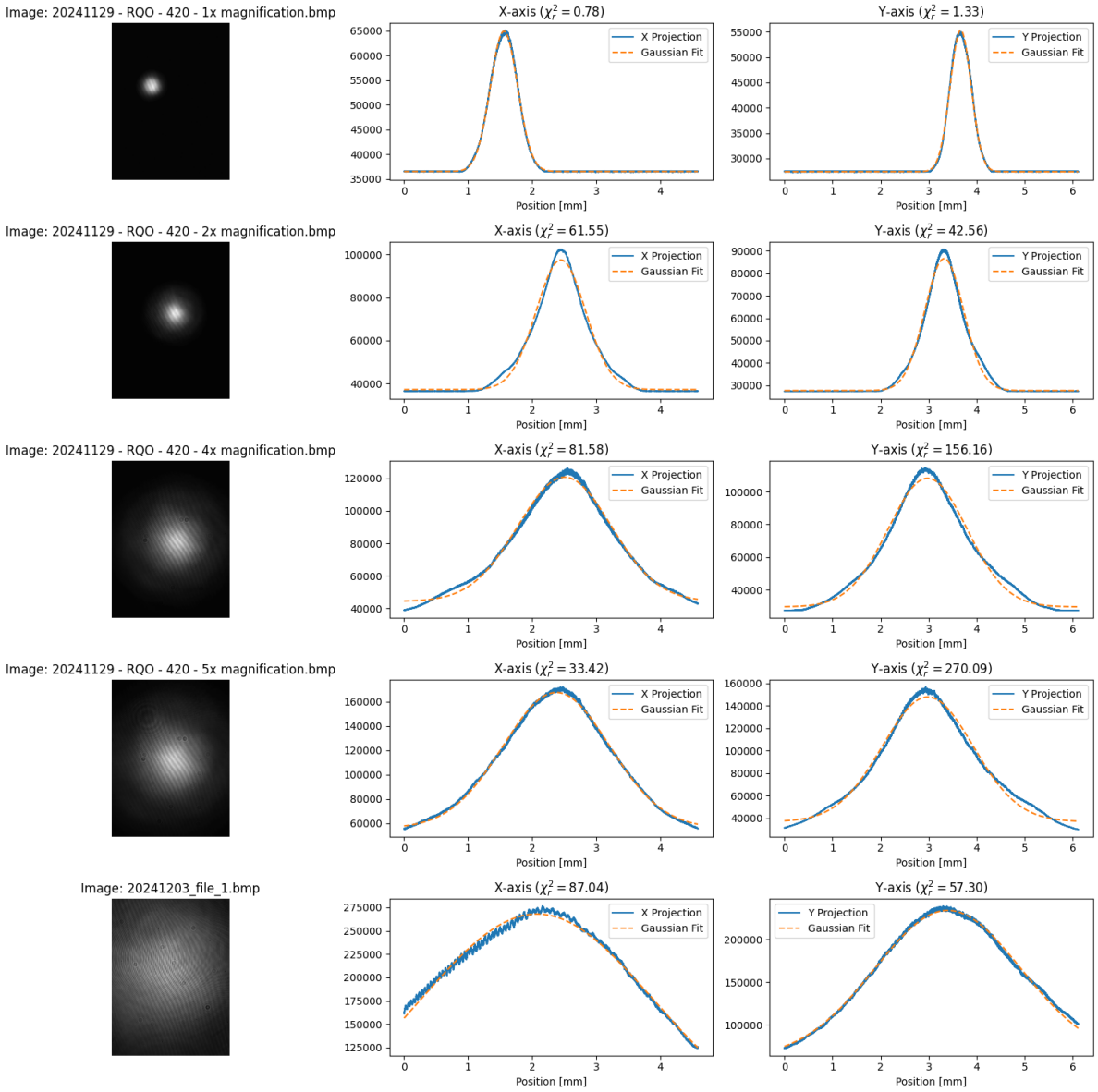

Figure A.1: Images of the laser beam taken by the Arducam for different magnifications. A Gaussian fit is applied to each dataset.

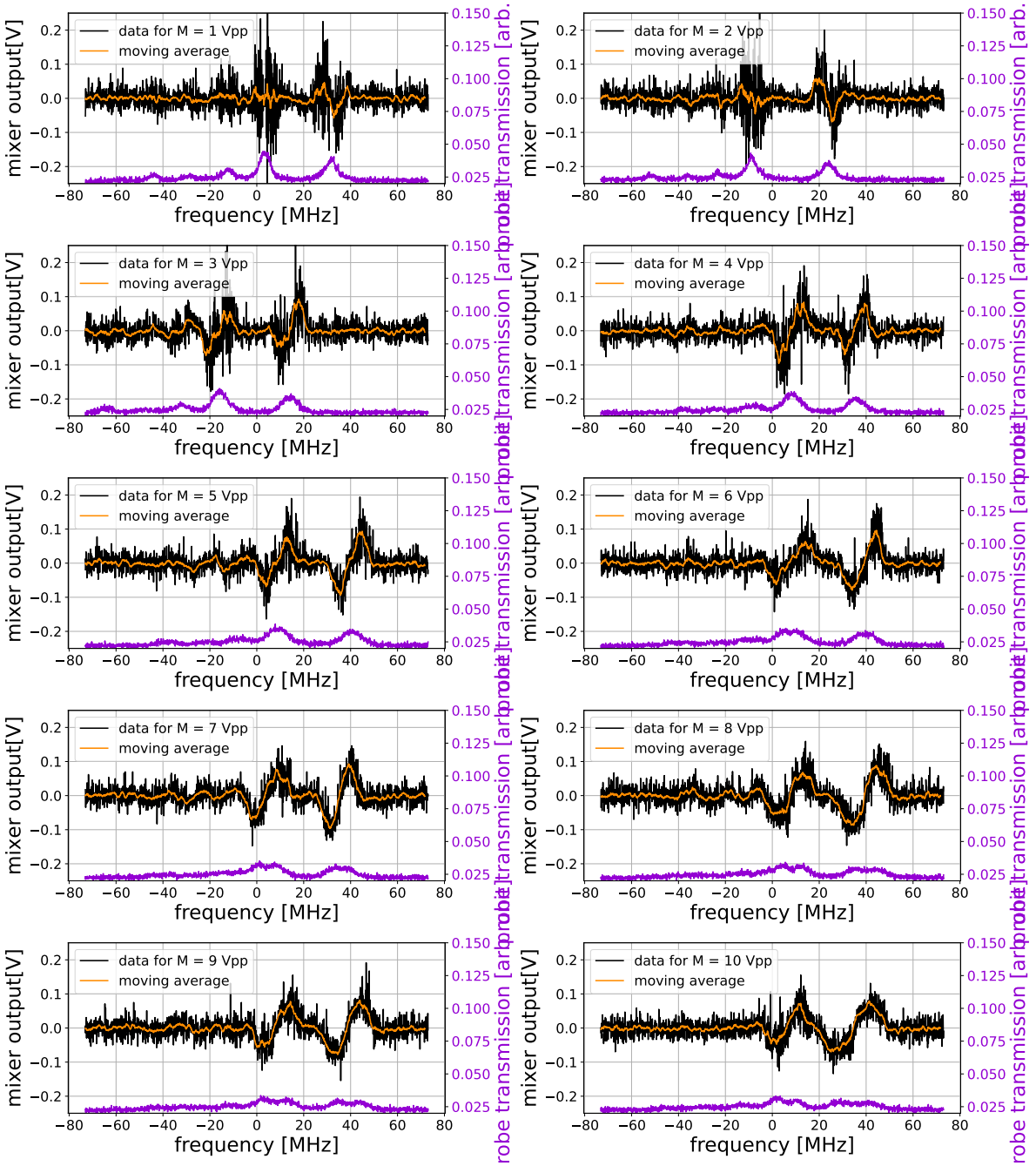

Figure A.2: Doppler free spectrum and error signals with moving average for different modulation amplitudes M

List of Figures

List of Tables